



HAL
open science

Identification and quantification of chemical reactions in a coastal aquifer to assess submarine groundwater discharge composition

Tybaud Goyetche, Linda Luquot, Jesus Carrera, Laura Martínez-Pérez,
Albert Folch

► To cite this version:

Tybaud Goyetche, Linda Luquot, Jesus Carrera, Laura Martínez-Pérez, Albert Folch. Identification and quantification of chemical reactions in a coastal aquifer to assess submarine groundwater discharge composition. *Science of the Total Environment*, 2022, 838 (1), pp.155978. 10.1016/j.scitotenv.2022.155978 . hal-03796089

HAL Id: hal-03796089

<https://hal.umontpellier.fr/hal-03796089>

Submitted on 17 Oct 2022

HAL is a multi-disciplinary open access archive for the deposit and dissemination of scientific research documents, whether they are published or not. The documents may come from teaching and research institutions in France or abroad, or from public or private research centers.

L'archive ouverte pluridisciplinaire **HAL**, est destinée au dépôt et à la diffusion de documents scientifiques de niveau recherche, publiés ou non, émanant des établissements d'enseignement et de recherche français ou étrangers, des laboratoires publics ou privés.

Title: Identification and quantification of chemical reactions in a coastal aquifer to assess submarine groundwater discharge composition

1 Tybaud Goyetche^{1,2,3*}, Linda Luquot⁴, Jesus Carrera^{1,2}, Laura Martínez Pérez^{1,2,3}, Albert
2 Folch^{2,3}

3 ¹ Institute of Environmental Assessment and Water Research (IDAEA), CSIC, Jordi Girona 18,
4 08034 Barcelona, Spain

5 ² Associated Unit: Hydrogeology group (UPC-CSIC)

6 ³ Department of Civil and Environment Engineering, Universitat Politècnica de Catalunya (UPC),
7 Jordi Girona 1-3, 08034 Barcelona, Spain

8 ⁴ Géoscience Montpellier, Université de Montpellier, CNRS, Montpellier, France

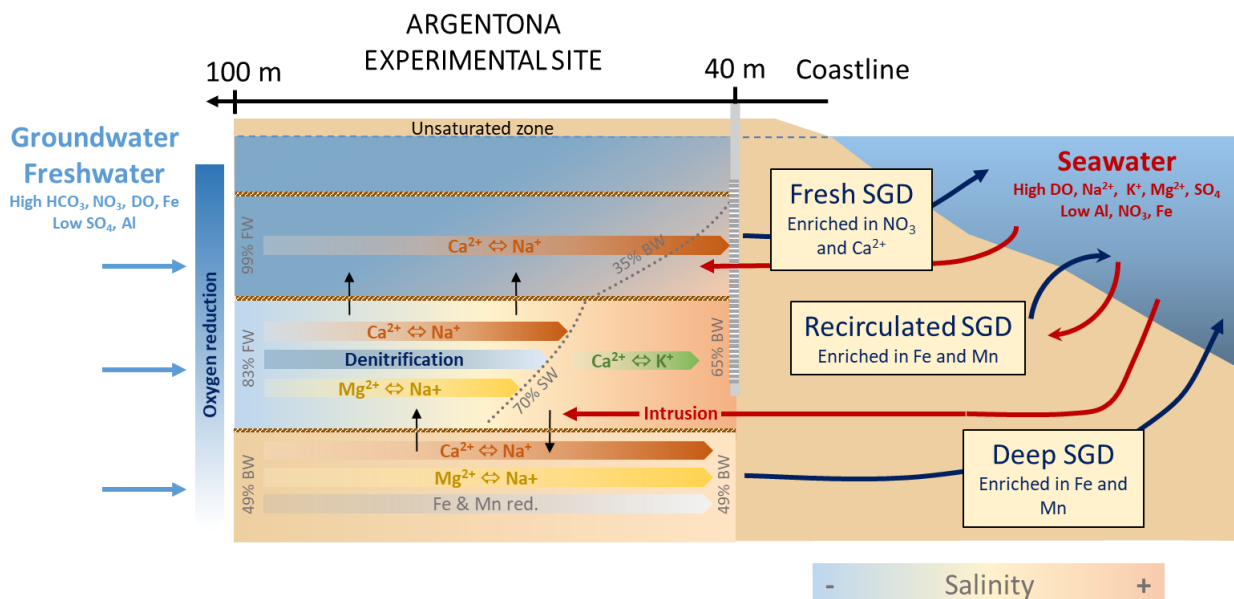
9 *Corresponding author:

10 Tybaud Goyetche

11 Institute of Environmental Assessment and Water Research (IDAEA), CSIC, Jordi Girona 18,
12 08034 Barcelona, Spain

13 e-mail: tgoyetche@gmail.com

Graphical abstract



14

Highlights

- 15 • Coastal aquifers deliver large nutrient quantities to the sea through SGD.
- 16 • FW and SW mixing promotes numerous chemical reactions.
- 17 • Chemical reaction quantification is essential to assess GW quality SGD composition.
- 18 • Coastal aquifers play a significant role in contamination reduction.

Abstract

19 In coastal aquifers, two opposite but complementary processes occur: Seawater
20 intrusion (SWI) and Submarine groundwater discharge (SGD). SWI may salinize
21 freshwater in exploited aquifers while SGD transports essential chemical elements to the
22 sea. Aquifers are expected to be chemically reactive, both because they provide abundant
23 surfaces to catalyze reactions and because mixing the very different Fresh Water (FW)
24 and SW should promote numerous reactions. Characterizing and quantifying these
25 reactions are essential to assess the composition of both aquifer water quality and
26 submarine groundwater discharge. Indeed, sampling SGD is difficult, so that its
27 composition is usually uncertain. We propose a reactive mixing methodology based on
28 principal component analysis to (i) identify the sources of water and possible reactions
29 occurring in the aquifer, and (ii) quantify mixing ratios and the extent of chemical
30 reactions. We applied this methodology to the Argenton coastal aquifer located North of
31 Barcelona. The aquifer contains fluvial sediments of granitic origin and overlies
32 weathered granite. Identification of end members (FW and SW) and the spatial
33 distribution of their mixing ratios illustrate the application procedure. The extent of
34 reactions and their spatial distribution allow us to distinguish reactions that occur as a
35 result of SWI. This is relevant for recirculated saltwater SGD. The most important
36 reaction is cation exchange, especially between Ca and Na, which promotes other

37 reactions such as gypsum and fluorite precipitation. Iron and Manganese are mobilized in
38 the SW portion but oxidized and precipitated in the mixing zone, so that Fe (up to 15
39 $\mu\text{Eq/L}$) and Mn (up to 10 $\mu\text{Eq/L}$) discharge is restricted to SW SGD. Nitrate is reduced
40 in the mixing zone. The actual reaction amounts are site specific, but the processes are
41 not, which leads us to conjecture the importance of these reactions to understand the SGD
42 discharge elsewhere.

Keywords

43 Grounwater; Coastal aquifer; Submarine Groundwater Discharge; Mixing model;
44 EMMA Analysis; Chemical reactions.

1. Introduction

45 Population density in coastal areas is almost three times higher than the global
46 average ([Small & Nicholls, 2003](#)). The impact of high population on freshwater (FW)
47 demand is very strong. One of its consequences is the intensification of seawater (SW)
48 intrusion (SWI) ([Alfarrah & Walraevens, 2018](#)). SWI is a natural coastal process that is
49 intensified where there is a significant extraction of freshwater. At the same time, coastal
50 aquifers discharge continental FW, largely mixed with SW in the aquifer, but also
51 recirculated SW ([Burnett et al., 2003](#)) towards the sea through Submarine Groundwater
52 Discharge (SGD). Some authors argue that the quantified volumes of SGD resulting from
53 either recirculated SW (i.e. SW exchange resulting from sea level fluctuations), mixed
54 FW and SW, or FW, are many times greater than the river discharge ([Taniguchi et al.,](#)
55 [2019](#)). SGD carries high solute and nutrients concentrations into the sea ([Slomp & Van](#)
56 [Cappellen, 2004](#)). Those elements may be important to submarine ecosystems ([Luijendijk](#)
57 [et al., 2020](#)), which lends an added relevance to the hydrochemistry of coastal aquifers.

58 The hydrochemistry of coastal aquifers depends not only on the nature of the
59 types of groundwater (end-members) that mix in these areas but also on their ensuing
60 interactions and reactions with the solid phases (Moore, 1999). Numerous studies indicate
61 the occurrence of chemical reactions in coastal aquifers including ion exchange, redox
62 reactions related to organic matter biodegradation, and mineral dissolution and
63 precipitation. Wigley and Plummer (1976) and Hanshaw and Back (1980) observed that
64 the mixing between freshwater (FW) and seawater (SW), both in equilibrium with calcite,
65 may tend to dissolve calcite, thus favoring coastal karst formation (Back et al., 1986;
66 Fratesi, 2013). The fact that calcite dissolution has been reported with only 2% of SW
67 (Magaritz et al., 1980), together with the fact that transport dynamics favor dissolution
68 on the freshwater side of the mixing zone (Rezaei et al., 2005), not only explain karst
69 development features, but also highlight the high reactivity that results from mixing so
70 different waters.

71 Cation exchange, driven by the invasion of SW, is frequently reported as a leading
72 geochemical process. A significant deviation of cations from conservative mixing
73 (increases in calcium and decreases in sodium, magnesium, and potassium) is usually
74 observed (Appelo & Willemssen, 1987; Giménez-Forcada, 2010; Gomis-Yagües et al.,
75 2000; Martínez & Bocanegra, 2002; Pulido-Leboeuf, 2004). Russak et al. (2016) used
76 field data and column experiments to study the effect of salinization and freshening cycles
77 on other minor cations Li^+ , B^- , Mn^{2+} and Ba^{2+} . Cation exchange, together with the
78 dissolution of some minerals, can promote the precipitation of others. This is the case for
79 dolomite and, especially, gypsum. In fact, a depletion in sulphate concentrations is
80 observed in a majority of works (Andersen et al., 2005; A. P. Barker et al., 1998;
81 Custodio, 1992; Gomis-Yagües et al., 2000). Sulphate reduction, which has also been
82 proposed, requires anoxic conditions and significant amounts of electron donors, which

83 may be caused by naturally occurring organic matter at the seabed or from polluted FW.
84 In fact, iron and manganese reduction has been described in the mixing zone where
85 microbial iron reduction has been proposed to account for most of the anaerobic
86 degradation of natural organic matter (Snyder et al., 2004).

87 These biogeochemical reactions explain that the composition of submarine
88 groundwater discharge differs from the one predicted by simple mixing of FW and SW
89 (Moore, 2010). They also explain that saline water returning to the sea due to sea-aquifer
90 exchange may be quite different from sea-water, which may help understanding sea
91 chemical balances and SGD. For instance, the global calcium balance in the ocean has
92 traditionally missed a significant input (Milliman, 1993; Wilkinson & Algeo, 1989),
93 estimated between 40 and 120% of the fluvial inflow (Sawyer et al., 2016). Most research
94 on SGD chemistry focuses on nutrients, which control primary production (Grzelak et al.,
95 2018; Liu et al., 2021; Valiela et al., 1990). It has been found that commercial fish,
96 aquaculture and lobster yields are positively correlated with terrestrial nutrients
97 discharged into coastal waters (Peng et al., 2021; Sutcliffe Jr, 1972). Nutrients, which are
98 essential elements for photosynthetic organisms and the ensuing trophic chains, may
99 become harmful for submarine ecosystems and lead to algal blooms when in excess
100 (Anderson et al., 2002; Chen et al., 2020; Luo & Jiao, 2016). Major ions cycles (Cl,
101 SO_4^{2-} , Na^+ , K^+ , Mg^{2+} , Ca^{2+} , and HCO_3^-) attract relatively less attention because they are
102 not limiting. Yet, they can exert a significant control on the chemical forcing in coastal
103 areas and stimulate primary production (Kłostowska et al., 2020; Liu et al., 2017; Santos
104 et al., 2008).

105 The large number and interdependence of chemical reactions in coastal aquifers
106 makes their hydrochemistry difficult to explain. Hydro-chemical studies in coastal

107 aquifers are usually qualitative: describing groundwater composition and conjecturing the
 108 reactions that may lead to measured concentrations. We suggest that quantifying such
 109 potential reactions is useful to confirm or discard conceptual models, strengthen the
 110 analysis, and help to build numerical models. The quantification is traditionally achieved
 111 through models, which also help to assess the response of the system to changing
 112 conditions. But reactive transport models are conceptually difficult, because of
 113 difficulties of transport and density dependent flow, and practically complex, because
 114 they require a large amount of data and long observation time-series. To simplify the
 115 numerical model implementation, it is mandatory to identify the most important reactions.

116 A preliminary approximation to the concentrations of chemical species can be
 117 achieved using mixing models. These are based on writing the concentration of any
 118 species i in a sample j (C_{ij}) as (Christophersen et al., 1990; Hassen et al., 2018; Jurado et
 119 al., 2015) :

$$C_{ij} = \sum_e \lambda_{ej} C_{ei} \quad (1)$$

120 where C_{ei} is the concentration of species i in the end-member e and λ_{ej} is the proportion
 121 of end-member e in the sample j . λ_{ej} must satisfy the following constraints:

$$0 \leq \lambda_{ej} \leq 1 \quad (2)$$

$$\sum_e \lambda_{ej} = 1 \quad (3)$$

122 Mixing ratios can be obtained from the samples and end-members concentrations
 123 using these equations. The solution is trivial in the frequent cases where only two end-
 124 members (FW and SW) are present. In these cases, the fraction of seawater in sample j
 125 (λ_{SWj}) is classically calculated from Cl concentration (Appelo & Postma, 2005):

$$\lambda_{SWj} = \frac{C_{Cl,j} - C_{Cl,FW}}{C_{Cl,SW} - C_{Cl,FW}} \quad (4)$$

126 The large difference between Cl^- concentrations or similar salinity indicators, such as
127 electrical conductivity, in FW and SW makes Eq. 4 quite robust and, thus, widely used.
128 Still, attention must be paid to measurement errors, which can be identified if other
129 species are used for the calculation of mixing ratios. For example, [Shin et al. \(2020\)](#)
130 reported some underestimations using Br ions compared with Cl ions. Therefore, the
131 chemical element chosen to calculate λ_{SWj} may be important. Conservative chemical
132 elements such as stable isotopes, or metals are used as SWI and/or SGD tracers ([Long &](#)
133 [Valder, 2011](#); [Nakaya et al., 2007](#)). Other tracers (i.e. Sr and Ra isotopes) may help in
134 computing mixing ratios but require specific sampling protocols and additional costs to
135 regular monitoring campaigns. Moreover, the use of these tools can be hindered when the
136 mixing between end-members is not clear, end-members composition vary with time or
137 when they are not identified ([Kendall & Caldwell, 1998](#), [Cerdà-Domènech et al., 2017](#)).

138 Identification of end-members is a conceptual problem. Often, they result from a
139 good hydrogeological characterization of the system. Nevertheless, identification can be
140 non-trivial in complex sites with multiple candidates for end-members. Identification is
141 greatly aided by End Member Mixing Analysis (EMMA, [Christophersen et al. \(1990\)](#);
142 [Hooper \(2003\)](#); [Hooper et al. \(1990\)](#); [Vázquez-Suñé et al. \(2010\)](#)). EMMA is a powerful
143 statistical method based on principal component analysis (PCA) that aims at explaining
144 the variability of a data set by reducing the dimensions of the problem by grouping
145 correlated variables. To do so, eigenvalues are calculated and then projected into a low-
146 dimensional space (2 or 3) by selecting the eigenvectors explaining most of the
147 variability. End-members should encircle all the other projected observation points,
148 which together with conceptual understanding helps in their identification. Once the end-

149 members have been identified, their mixing ratios in each sample can be evaluated.
150 EMMA is an adequate technique, but cannot be directly applied to species that undergo
151 some reaction. Therefore, a fairly widespread EMMA rule is to keep only the conservative
152 species in the analysis (Li et al., 2016; Tubau et al., 2014), which is a limiting factor when
153 many reactions occur and affect most species. This is particularly the case FW and SW
154 mix, even if both are in equilibrium with the host sediments such as in coastal aquifers.

155 Including reactions in mixing calculations has been addressed by several
156 researchers. Tubau et al. (2014) and Jurado et al. (2015) considered reactions as end-
157 members by adding, for every reaction, an artificial end-member with the species
158 participating in the reaction. Unfortunately, this approach does not properly represent
159 mixing in the aquifer since the calculated mixing ratios do not add up to one (Eq. 3) and
160 the identification of actual reactions remains unclear. Pelizardi et al. (2017) present a
161 methodology to formalize mixing ratio calculations, which can be rewritten as:

$$C_{ij} = \sum_e \lambda_{ej} C_{ei} + \sum_e S_{ir}^t R_{rj} \quad (5)$$

162 where S_{ir} is the stoichiometric coefficient of species i in reaction r and R_{rj} is the reaction
163 extent of reaction r in sample j . That is, R_{rj} should be understood as the amount
164 (expressed in moles or equivalents per liter) of reaction r reactants that have gone
165 products in sample j . The method consists of several steps: (i) use the EMMA to identify
166 the species participating in reactions and determine the associated reactions, (ii) define
167 conservative components u associated with the reactions identified in the previous step
168 (De Simoni et al., 2005), (iii) repeat the EMMA process with the conservative
169 components for the identification of end-members and (iv) calculate the mixing ratios in
170 each sample. The method is appealing because it formalizes the gist of hydrology (e.g.,
171 Davis and DeWiest (1966); Hurrell et al. (2013)): understanding water exchanges among

172 compartments (first term in Eq, 5) and the processes it undergoes (second term). Still, the
173 method does not specify how to quantify the reactions (R_{rj}), and the methodology needs
174 refinements on how to identify the reactions to be applied to real data (Pelizardi et al.
175 (2017) examples are synthetic).

176 The objective of this work is double. First, we want to refine the reactive EMMA
177 methodology and apply it to a complex real case influenced by SWI (the Argenton site,
178 Martínez-Pérez et al. (2022)). Second, we want to identify and quantify hydrochemical
179 processes at this coastal site to understand the chemistry of SGD.

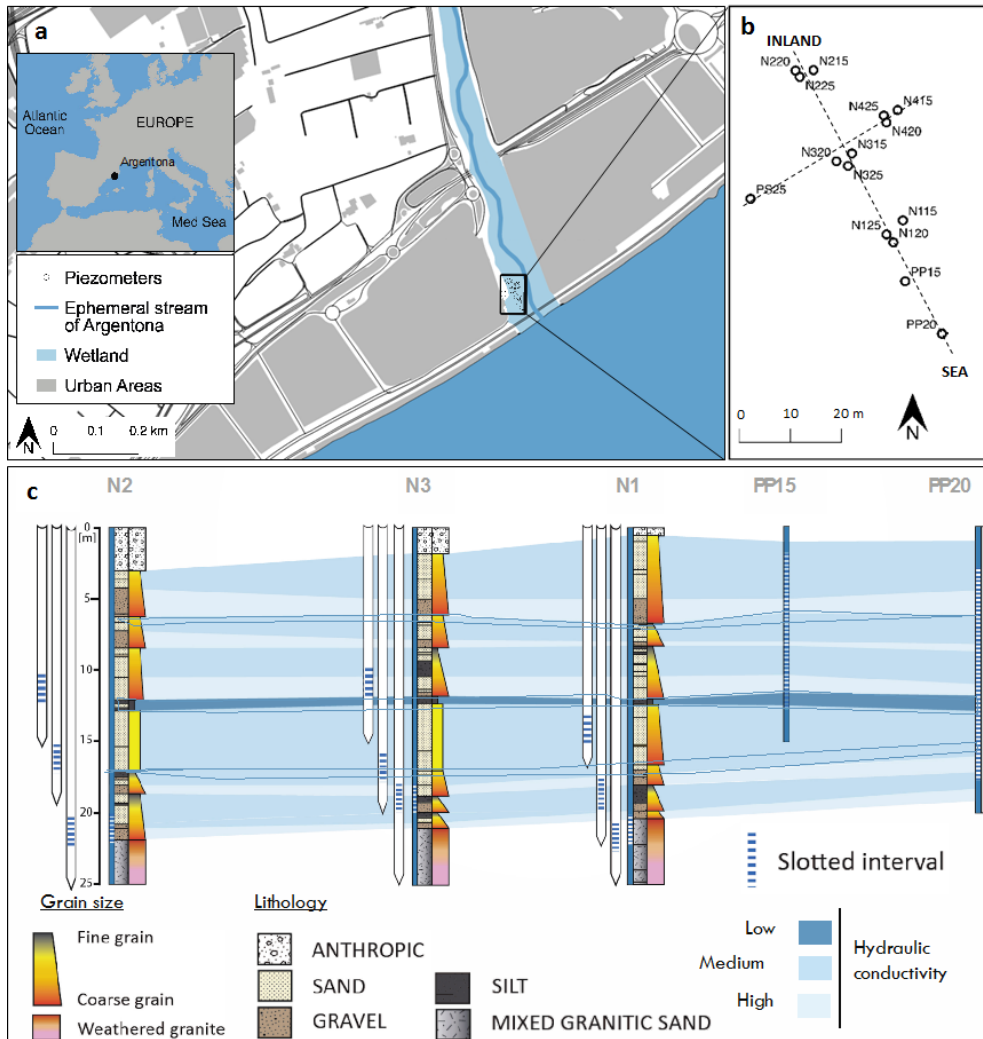
2. Materials and methods

180 2.1. Study site, sampling, and analytical techniques

181 We use chemical data from the well-instrumented Argenton Experimental Site
182 (Folch et al. 2020) located 30 km north of Barcelona (Spain), at the mouth of the
183 Argenton ephemeral stream (Figure 1). This site is characterized by a dynamic SWI and
184 SGD, which leads to an active mixing zone (Martínez-Pérez et al., 2022). The site climate
185 is Mediterranean, with dry summers and mild, wet winters. Rainfall (some 600 mm/year)
186 concentrates mainly during autumn and spring. It controls the Argenton stream flow and
187 the alluvial aquifer recharge.

188 The site aims at monitoring seawater intrusion dynamics at different depths thanks
189 to 15 wells. 12 of them form 4 nests with 2 m screened intervals at 3 different depths (15,
190 20, and 25 m). They are labeled Nx-15, Nx-20, and Nx-25 where x is the nest number (1
191 to 4). 3 other solitary boreholes complete the experimental site: PS-25 with a 2 m screened
192 zone at 25 m depth and 2 fully screened boreholes of respectively 15 and 20 m depth (PP-
193 15 and PP-20). The site is 100 m long inland from the coastline and 30 m wide.

194 The aquifer system is formed by alluvial deposits with an alternation of gravel,
195 sands, and silty layers over a weathered granitic substratum. Mineralogy composition was
196 measured through XRD at different depths and indicates a majority of silicates as Quartz
197 (13–37%, SiO₂), Microcline (10–34%, KAlSi₃O₈), Albite (21–46%, NaAl Si₃O₈) and Fe
198 rich Mg-hornblende (3–7%). Some clay minerals, such as Illite, are also observed with a
199 fairly wide range depending on the depth (3–38%) (see details in [Martínez-Pérez et al.](#)
200 [\(2022\)](#)). The anthropogenic impact in the watershed is quite significant with urban,
201 agricultural, and industrial areas that can have an impact on groundwater quality ([Ruff-](#)
202 [Salís et al., 2019](#)). Both the geological background and human activities in the watershed
203 may foster reactions associated with the above minerals such as silicate alterations, cation
204 exchange, and some organic matter degradation.



205

206 Figure 1: Experimental site of Argentona: (a) location, (b) borehole distribution, and (c) aquifer
 207 system (Modified from [Martínez-Pérez et al. \(2022\)](#))

208 Groundwater is sampled using submersible pumps (Gigant Submersible Pumps,
 209 Van Walt). A purging step is first applied by pumping at least three times the volume of
 210 the piezometer. Groundwater samples are then collected following a strict protocol and
 211 stored in pre-sanitized bottles. Sampling bottles had been previously washed with diluted
 212 nitric acid and rinsed with distilled water in the laboratory. Then in the field, each bottle
 213 is rinsed three times with groundwater before sampling and every other precaution is
 214 taken (use of gloves, handling one sample at a time, cleaning of utensils between taking
 215 each sample...) to avoid contamination. Electrical conductivity (EC), pH, temperature,
 216 Eh, and dissolved oxygen are measured on-site with a YSI multiparameter probe,

217 previously calibrated with standard solutions. These measurements are made through a
218 flow cell to directly pass groundwater across sensors to avoid contact with ambient air
219 and prevent degasification or mineral precipitation. Alkalinity (as HCO_3^-) is analyzed
220 manually by titration evaluation with sulfuric acid, accounting for the pH of the sample.

221 Table 1 summarizes the species analyzed for this study and the analytical method
222 and laboratory. The water samples used for this study were collected during the field
223 campaign of winter 2016 (presented in [Martínez-Pérez et al. \(2022\)](#)). As rains mainly
224 occurs in autumn, we expect high FW content in groundwater samples. See
225 supplementary materials for the full chemical dataset.

226 As the selected site is a coastal aquifer affected by SWI and SGD, the expected
227 end-members for the mixing zone are, at least, one freshwater end-member representing
228 the global aquifer water and seawater end-member (for the SWI part). As a representation
229 of such end-members, we considered a well located on the Argentona watershed upper
230 part for the freshwater (F1) and seawater (SW) from the nearby coast. To constrain all the
231 possible water inflows in the Argentona site and to be sure to not exclude any potential
232 end-members, we also sampled the ephemeral stream during a rainfall event (STREAM)
233 and the wastewater treatment plant effluent (SEWAGE) that discharges in the sea near
234 the experimental site.

235

Table 1 : Chemical species considered, analysis method, and laboratories of analysis.

Chemical species	Symbol	Analysis Method	Laboratory	
Chloride	Cl^-	Ion	Catalan Institute for Water Research (ICRA)	
Sulphate	SO_4^{2-}	Chromatography		
Nitrate	NO_3^-	(IC)		
Calcium (Ca)	Ca^{2+}		Institute of Environmental Assessment and Water Studies (IDAEA)	
Sodium (Na)	Na^+			
Magnesium (Mg)	Mg^{2+}			
Potassium (K)	K^+			
Manganese (Mn)	Mn^{2+}	Inductively		
Iron (Fe)	Fe^{2+}	Coupled Plasma –		
Fluorine (F)	F^-	Mass Spectrometry		
Silicon (Si)	Si^{4+}	(ICP-MS)		
Barium (Ba)	Ba^{2+}			
Bromine (Br)	Br^-			
Aluminium (Al)	Al^{3+}			
Lithium (Li)	Li^+			
$\delta^{18}O$ and δD	$\delta^{18}O$ and δD			University of Barcelona (UB).
Alkalinity (as HCO_3^-)	HCO_3^-	Titration-based		Field measurement
Electrical conductivity	EC	YSI multiparameter meter	Field measurement	
Dissolved Oxygen	O_2	YSI multiparameter meter	Field measurement	

2.2. Identification and quantification of chemical reactions

We propose a three step procedure for the identification and quantification of chemical reactions using reactive mixing calculations:

- (1) Reactive EMMA for identification of reactions and end-members
- (2) Mixing calculations
- (3) Quantification of chemical reactions

These steps are detailed below.

244 **2.2.1. Step 1: Reactive EMMA for identification of reactions and end-members**

245 Interpretation and representation of hydrogeochemical data may be complex
246 because of the large number of compounds and their time evolution. To simplify the
247 analysis, the whole chemical data set is presented as a concentration matrix (X) ($n_s \times n$,
248 where n_s is the number of chemical species and n is the number of samples). We used
249 the application of EMMA-MIX (Carrera et al., 2004) to select end-members, evaluate the
250 mixing ratios between different end-members and quantify the reactions occurring in the
251 coastal aquifer of Argentina.

252 The identification of chemical reactions and end-members follows an iterative
253 process, summarized in Figure 2:

254 **Preliminary analysis:** EMMA (Carrera et al., 2004) is applied to the original matrix X
255 resulting from raw concentration data.

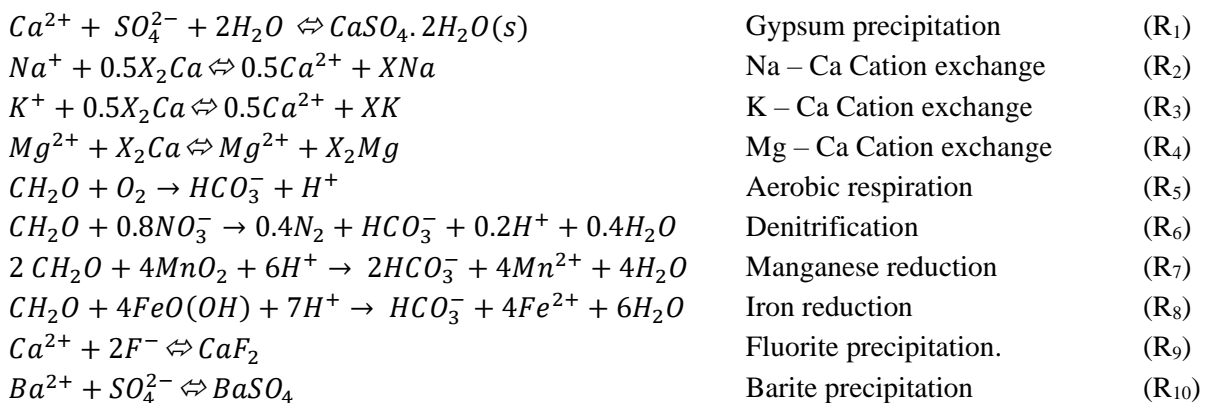
256 **Step a: Propose candidate reactions:** this is done by (1) conceptual analysis (some
257 reactions, e.g., cation exchange may be expected to occur), (2) identification of
258 species possibly participating in reactions by checking differences from expected
259 conservative mixing behaviour. For example, the eigenvector associated to FW-SW
260 mixing typically display contributions of around $1/\sqrt{n_s}$ for conservative species
261 but not for those affected by chemical reactions, which tend to display a reduced
262 contribution. Another typical example is the case of eigenvectors without clear end-
263 members, but involving few species, which might come from a reaction (e.g., an
264 eigenvector with large contributions to Ca^{2+} and SO_4^{2-} can indicate gypsum
265 dissolution-precipitation).

266 **Step b: Build the stoichiometric matrix of the proposed reactions.** This matrix
 267 ($n_r \times n_s$, where n_r is the number of proposed reactions) includes the stoichiometric
 268 coefficient associated to species participating in the reactions.

269 **Step c: Derive components** (i.e., combinations of species that remain unchanged by the
 270 proposed reactions). This involves (1) computing the components matrix U ($n_s -$
 271 $n_r \times n_s$) from the stoichiometric matrix (see details in [Pelizardi et al. \(2017\)](#) and
 272 [Molins et al. \(2004\)](#)), and (2) multiplying the vector of concentrations of all species
 273 in each sample by the components matrix. This leads to a new data matrix, $X_u =$
 274 $U \cdot X$. In practice, this reduced data matrix results from eliminating the species
 275 involved in the reactions and replacing them with the corresponding components u ,
 276 while keeping the species that do not participate in any reaction.

277 **Step d: Conservative EMMA analysis:** EMMA is repeated using X_u . In case new
 278 reactions are identified, the procedure is repeated until a significant percentage of
 279 the variance (say, more than 90%) can be explained by a few eigenvectors and the
 280 data projections are encircled by conceptually reasonable end-members.

281 In our analysis, described in detail in section 3.1, we identified 12 potential
 282 reactions in agreement with the geological context and human activities around the
 283 experimental site affecting our system:





284 The 2 conservative components resulting from these reactions are:

$$u_1 = [Ca^{2+}] - [SO_4^{2-}] + 0.5[Na^+] + 0.5[K^+] + [Mg^{2+}] - 0.5[F^-] + [Ba^{2+}] + 1/6[Si^{4+}] \quad (6)$$

$$u_2 = [HCO_3^-] + [DO] + 1.25[NO_3^-] + 0.5[Mn^{2+}] + 0.25[Fe^{2+}] \quad (7)$$

285 where u_1 corresponds to the reactions associated to cation exchange and minerals
 286 dissolution-precipitation affecting $[Ca^{2+}]$ while u_2 is associated to $[HCO_3^-]$ and redox
 287 reactions. So, X_u is the matrix ($8 \times n$) containing the two above components and the
 288 remaining species not participating in reactions ($[\delta^{18}O]$, $[\delta D]$, $[EC]$, $[Br^-]$, $[Li^+]$ and
 289 $[Cl^-]$).

290 2.2.2. Step 2: Mixing calculations

291 Once the end-members for each sample are identified using EMMA, mixing ratios
 292 can be calculated using the MIX code (Carrera et al., 2004). A feature of this code is that
 293 it acknowledges that the uncertainty of end-member compositions may be greater than
 294 that of the actual samples. In essence, it is assumed that the measured concentrations,
 295 C_{mij} , of species in sample j results from conservative mixing of n_e end-members (Eq. 1)
 296 plus a measurement error and that the measured concentrations of end-members, C_{mei} ,
 297 also contain errors. That is,

$$C_{mij} = \sum_{e=1}^{n_e} \lambda_{ej} C_{ei} + \varepsilon_{mij} \quad i = 1, n_s; j = 1, n_m \quad (8a)$$

$$C_{mei} = C_{ei} + \varepsilon_{ei} \quad i = 1, n_s; e = 1, n_m \quad (8b)$$

298 where ε_{mij} and ε_{ei} are the measurement errors of concentrations of mixtures (samples)
 299 and end-members, respectively. Mixing ratios, λ_{ej} , and end-member concentrations, C_{ei} ,
 300 are obtained by minimizing the objective function:

$$F_{obj} = \sum_{i=1}^{n_s} \sum_{j=1}^{n_m} \left(\frac{\varepsilon_{mij}}{\sigma_{ij}} \right)^2 + \sum_{i=1}^{n_s} \sum_{e=1}^{n_e} \left(\frac{\varepsilon_{ei}}{\sigma_{ei}} \right)^2 \quad (9)$$

301 where σ_{ij} and σ_{ei} are the standard deviations of ε_{mij} and ε_{ei} respectively. These are the
 302 only data that needs to be specified, in addition to actual measurements, to run MIX. Here
 303 we have assigned by default a standard deviation of 0.1 times the measured concentration
 304 ($\sigma_{ij} = 0.1C_{ij}$), except for very small concentrations ($C_{mij} < 0.1\sigma_{si}$, where σ_{si} is the
 305 standard deviation of species i in all measurements), in which case $\sigma_{ij} = 0.01\sigma_{si}$. The
 306 same criterion was initially applied to end-members. Variances can be adjusted to broaden
 307 or restrict the concentration calculations. To this end, it is convenient to verify the
 308 deviation of both end member and sample concentrations from the raw data to ensure that
 309 the projections of calculated end-members over the selected eigenvectors using EMMA
 310 (Figure 2e) encircle the samples. Otherwise, σ_{ei} can be adjusted so that the concentrations
 311 of the end-members do not deviate too much from conceptual expectations and the
 312 distribution is preserved.

313 In our case, we had to adjust σ_{ei} for the F1 sample for Cl^- and u_1 . The initial
 314 values are respectively: 7.210 mmol/L \pm 51.98 mmol/L and 1.881 mmol/L \pm 528.59
 315 mmol/L.

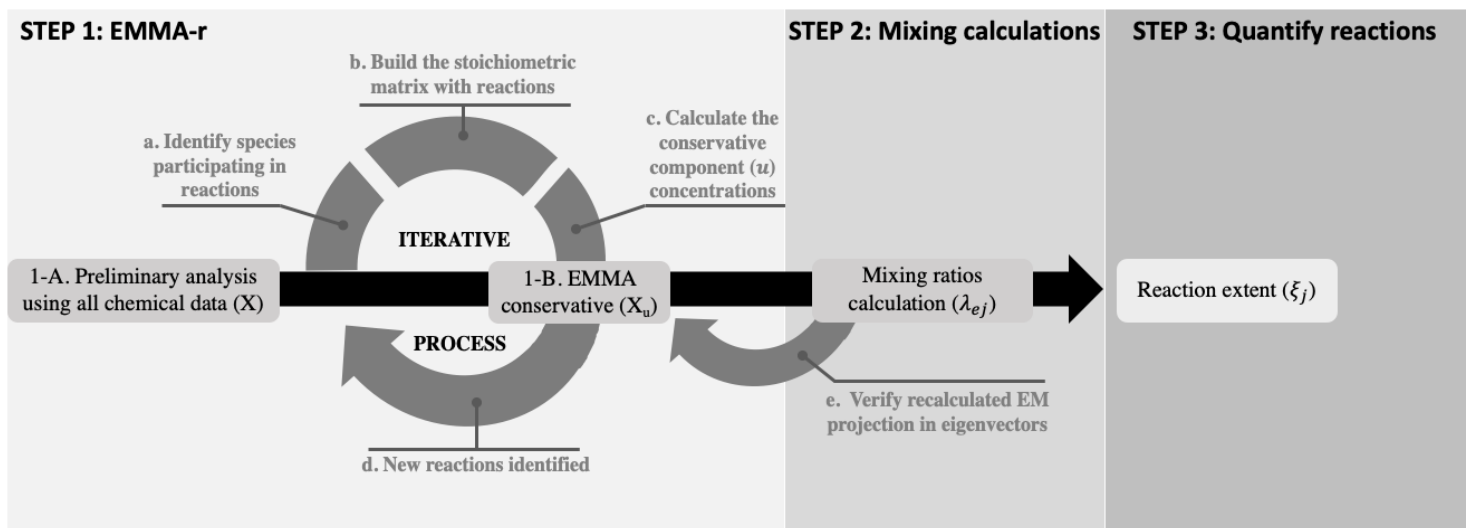
316 2.2.3. Step 3 : Quantification of chemical reactions

317 Once the e end-member proportions in sample j (λ_{ej} , Eq. 1) are calculated, we
 318 can quantify the extent of reaction R_{rj} in sample j (Step 3, Figure 2) from the

319 concentration of the secondary species associated to the reaction r (Eq. 4). We take
 320 advantage of the fact that we have built the stoichiometric matrices in such a way that a
 321 secondary species can only result from specific reaction. Therefore, the reaction extent
 322 R_{rj} of reaction r in sample j is equal to considering conservative mixing, the deviation
 323 from the measured concentration of species i ($C_{i_{Meas.}}$) from the conservative mixing
 324 concentrations (C_{rjm}) can be defined as (Eq. 5).

$$R_j = [C_{i_{Cons.}}] - [C_{i_{Meas.}}] \quad (0-10)$$

325 where $[C_{i_{Cons.}}]$ is calculated using λ_{ej} according to Eq. 1, as if there were no reactions
 326 (conservative mixing).



328 Figure 2: EMMA reactive flow chart for the end-member identification and chemical reactions
 329 quantification

3. Results and discussion

330 3.1. Step 1: Chemical reactions for end-member identification

331 In this section, we detail how we obtained the final chemical system applying the
 332 EMMA. We start (iteration 0) by consider all chemical species in Table 1 The goal is to
 333 reduce the set of species and components through invoking reactions so as to explain.

334 Second, an iterative process begins until the variance by the least number of eigenvectors.
 335 Moreover, end-members must enclose the chemical composition of our system. Table 2
 336 presents the parameters for each iteration and the results of the variance explained by EG1
 337 and EG2.

338 Table 2 : Parameters varying in each iteration to identify chemical reactions using EMMA. Where
 339 n_r is the number of reactions considered, R_n the reaction identifier, n_s is the number of species
 340 considered, n_u is the number of conservative components, $W = \sqrt{1/(n_s + n_u)}$ is the theoretical
 341 contribution of each species, if all species and components were equally weighted, and n_e is the
 342 number of potential end-members identified.

Iteration number	0	1	2	3	4
n_r	0	4	8	11	12
R_n	-	R ₁ to R ₄	R ₅ to R ₈	R ₉ to R ₁₁	R ₁₂
n_s	20	15	10	6	6
n_u	-	1	2	3	2
W	0.22	0.25	0.29	0.33	0.35
n_e	>4	4	4	3	2
EG1 contribution (%)	67.47	62.87	73.03	87.12	96.73
EG2 contribution (%)	11.53	13.96	11.50	10.43	2.10

343 Iteration 0 or preliminary analysis starts by applying the EMMA to the original
 344 chemical data without reactions (i.e., 20 x 18 matrix, both n_r and n_u are set to zero in
 345 Table 2). The two first eigenvectors explain 79% of the variance (Table 2). As shown in
 346 Figure 3a, EG1 represents the mixing between a freshwater end-member (FW) and the
 347 saline end-member (SW). However, we observe that many chemical species are affected
 348 by other processes than mixing. That is, their contribution is not equal to the theoretical
 349 contribution W of each species and components (with $W = \sqrt{1/(n_s + n_u)}$) if all were
 350 equally weighted (the values are shown in Table 2 and indicated in Figure 3, top row).
 351 Moreover, results show that more than two end-members are needed to explain a

352 significant portion of the data variability ($n_e > 4$, see Figure 3c). The results from this
353 preliminary iteration (Iteration 0) imply that we must acknowledge chemical reactions to
354 interpret groundwater hydrochemistry.

355 To acknowledge reactions, the first reactive EMMA (EMMA-reactive
356 hereinafter) iteration (Iteration 1) includes cation exchange reactions (R2 to R4, Na^+ ,
357 K^+ and Mg^{2+} with Ca^{2+}) as they represent the main type of reaction occurring in non-
358 karstic coastal aquifers (Russak & Sivan, 2010). We also included gypsum precipitation
359 (R1) because it is frequently observed and because groundwater composition at the
360 Argenton experimental site is depleted in SO_4^{2-} (Martínez-Pérez et al., 2022). Note,
361 however, that results from the preliminary analysis (Iteration 0) did not suggest that the
362 species participating in cation exchange or gypsum precipitation Na^+ , K^+ , Mg^{2+} ,
363 SO_4^{2-} and Ca^{2+} , (indicated by a square in Figure 3a) are affected by any chemical reaction.
364 Despite this, we have decided to include R1 to R4 in iteration 1 to highlight the importance
365 of the conceptual model and the robustness of EMMA, allowing us to analyze and discuss
366 the validity of chemical reactions.

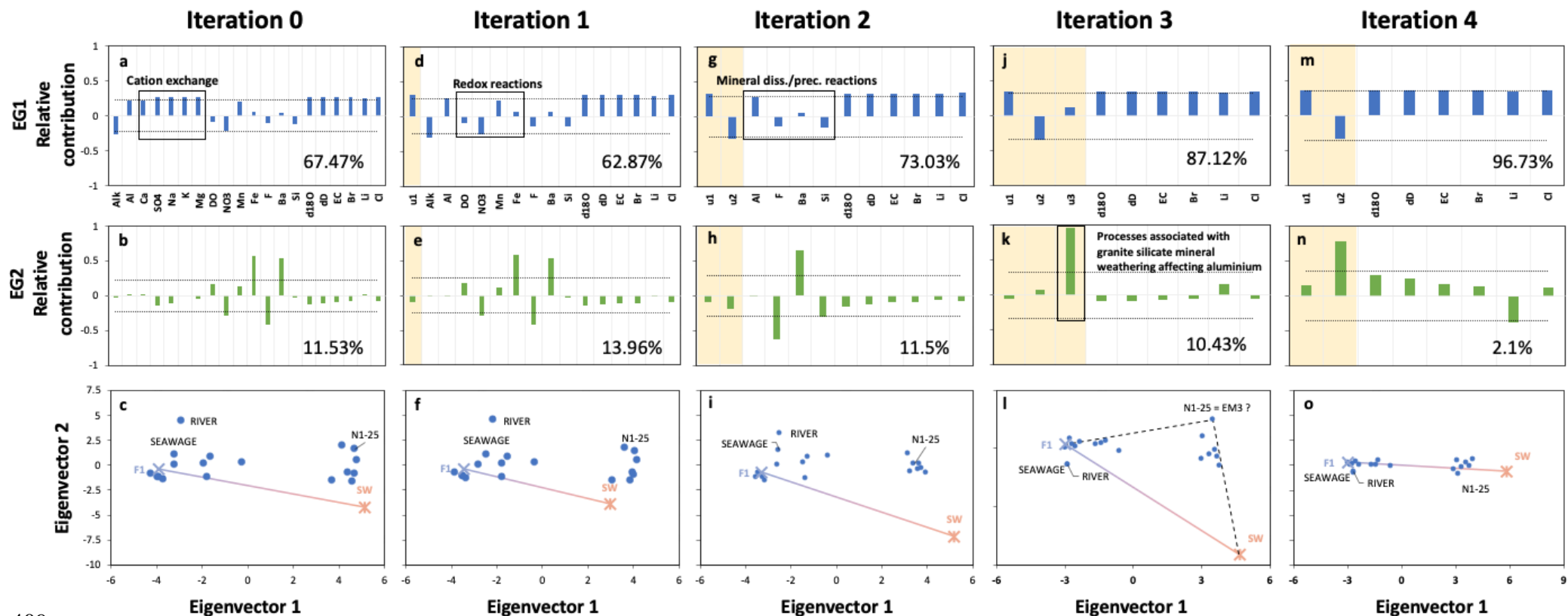
367 Reacting species are eliminated from the data matrix X during EMMA-reactive
368 iterations. Instead, conservative components (i.e. combinations of reactive species that
369 remain unaffected by reactions) are added to X. In iteration 1, the conservative component
370 resulting from cation exchange and gypsum precipitation is: $u_1 = Ca^{2+} - SO_4^{2-} +$
371 $0.5Na^+ + 0.5K^+ + Mg^{2+}$ (see Supplementary Material). Results of iteration 1
372 demonstrate two things: (i) the variance explained by the first two eigenvectors is reduced
373 to 77%, with a reduction of the EG1 relative contribution (see the difference with iteration
374 0 in Table 2); and (ii) we are still not able to identify end-members (Figure 3f). This lack
375 of improvement reflects that we are not following the EMMA recommendations (i.e.

376 reduced contribution to the eigenvector representing mixing) when considering chemical
377 reactions. In our case, EMMA suggests that we should consider other reactions first and
378 possibly add R1 to R4 in a later iteration. Consequently, we added redox reactions
379 affecting DO , NO_3^- , Mn^{2+} , and Fe^{2+} (indicated in Figure 3d) for iteration 2.

380 Adding redox reactions (R5 to R8) makes the chemical system more complex,
381 with 8 chemical reactions ($n_r = 8$, Table 2) that lead to a second conservative component
382 ($u_2 = HCO_3^- + DO + 1.25NO_3^- + 0.5Mn^{2+} + 0.25Fe^{2+}$) besides u_1 , obtained from the
383 previous iteration (see Supplementary Material). With two eigenvectors we are able to
384 explain up to 85% of the variance (i.e., a of 6% gain over iteration 0). Nevertheless, it
385 remains difficult to identify end-members (Figure 3i). New reactions are suggested by
386 EG1, affecting Al^{3+} , F^- , Ba^{2+} , and Si^{4+} (see Figure 3g). These species and the mineral
387 composition of the Argenton site, suggest adding fluorite, barite and feldspar mineral
388 dissolution-precipitation reactions (R9 to R11). This leads to a third conservative
389 component that $u_3 = Al^{3+} + 1/3 Si^{4+}$ (see Supplementary Material). u_3 represents the
390 weathering of the granitic minerals present in the Argenton aquifer. Note that, since
391 calcium and sulfate are already part of u_1 , fluorite and calcite precipitation imply treating
392 F^- and Ba^{2+} as secondary species and modifying u_1 , which now reads : $u_1 = Ca^{2+} -$
393 $SO_4^{2-} + 0.5Na^+ + 0.5K^+ + Mg^{2+} - 0.5F^- + Ba^{2+} + 1/6Si^{4+}$ and u_2 is unchanged.

394 The iterative process is repeated for a third time. According to this chemical
395 system with 11 chemical reactions ($n_r = 11$), we explain 98% with 2 eigenvectors. This
396 iteration gives better results than all the previous ones (+19% compared to iteration 0,
397 Table 2). However, end-members identification remains unclear since it would be
398 necessary to include 3 end-members to explain the data (F1, SW, and N1-25 as suggested
399 in Figure 3l). The presence of 3 end-members in a case of seawater intrusion is not

400 unusual and has been described in several cases of study in the literature considering
401 different freshwater sources or some fossil seawater (Chatton et al., 2016; Eissa, 2018;
402 Kim et al., 2017; Sivan et al., 2005; Wicks & Herman, 1996). In our system, we see that
403 EG2 is mainly controlled by u_3 which corresponds to the granitic weathering. The fact is
404 that if R11, takes place, for each mole of weathered potassic feldspar, 3 moles of Si^{4+} and
405 1 mole of Al^{3+} should be added to the solution. But Al^{3+} is unstable in solution at pH >
406 5, which suggests that Aluminium should be precipitating. The questionable nature of the
407 third end-member and the excess of Al^{3+} prompted us to perform a 4th iteration by adding
408 Gibbsite (Aluminium hydroxide) precipitation (R12), (see Supplementary Material).



409

410

411 Figure 3 : Results of the EMMA iterative process for the identification of chemical reactions and end-members. Columns represent the iterations from left to

412 right, going from 0 to 4, with the increasing number of reactions included in the chemical system. (1) species relative contribution to Eigenfactor 1; (2) species

413 relative contribution to Eigenfactor 2 and (3) EMMA projection of concentration data defined by eigenfactors 1 and 2. Yellow vertical bands represent the

414 number of conservative components involved in each iteration process.

415 This iteration proved to be the last one as it improved results, with 99% of the variance
416 explained by the first 2 eigenvectors. But the greatest improvement is seen in Eigenvector 1
417 (EG1, Figure 3m), which explains almost 97%. Furthermore, we observe that almost all the
418 species contribute equally with a relative weight of 0.35 ($\approx \sqrt{1/(n_s + n_u)}$), except u_2 which
419 is anticorrelated (-0.35). As we indicated before, the EG1 direction is controlled by the mixing
420 between freshwater and seawater. Accordingly, the u_2 anticorrelation with EG1 is quite
421 consistent since the chemical species constituting u_2 (HCO_3^- , DO , NO_3^- , Mn^{2+} , Fe^{2+} , F^-) are
422 representative of the freshwater with respect to other species. Moreover, in this last iteration,
423 the relative contribution of Eigenvector 2 is reduced to 2% (see the reduction from iteration 0
424 to 4 in Table 2). EG2 is mainly characterized by the conservative component u_2 with a relative
425 weight of 0.79. We consider the relative contribution of the remaining eigenvectors irrelevant
426 since EG2 represents only 2% of the variance. From these results, the end-members are
427 identifiable in the projection of sampling points using the first two eigenvectors. We observe
428 an alignment of the points in the mixing line between F1 (freshwater end-member) and SW
429 (Figure 3o).

430 **3.2.Step 2: Mixing ratios and recalculated end members**

431 Based on the iteration process, the model with 2 end-members (Iteration 4, Table 2) has
432 been chosen for our data set. End-members exact composition of end-members is recalculated
433 using the MIX code (Carrera et al., 2004) together with mixing ratios for each sample (Step 3,
434 Figure 2). Table 3 presents the recalculated composition of end-members.

435 For F1_r, the code tends to reduce concentrations, more specifically for Li , Br , u_1 , and
436 EC . Changes are respectively: -100% (irrelevant concentration $1.44 \cdot 10^{-6}$ mmol/L), -63%, -61%,
437 -31%. This reduction suggests that the actual end-member might be closer to rainfall than any
438 of our samples. In reality, MIX changes the concentrations to ensure that in this way, F1_r and

439 SW_r encircle all the other samples in the projection of EG1 and EG2 (not presented here as it
 440 overlays with the initial end-members). In the same way, to bring F1 closer to wells Nx-15 in
 441 EG1 and EG2 projections, a slight increase in $\delta^{18}O$ and δD with respectively 3.6% and 2.4%.
 442 While for SW_r, the most impacted concentrations are *Li* and *u*₂. The code tends to lower them
 443 respectively by 58% and 48%. Furthermore, the EC rises from 53.00 mS/cm to 56.89 mS/cm.

444 The MIX code takes into account the variance indicated by the user to recalculate the
 445 end-members. As mentioned before, as we were quite in agreement with the end-members
 446 initial position, we had to reduce the degree of freedom for two species in F1: *u*₂ and *Cl*⁻. So
 447 that the code does not change too much the concentrations. In the case of totally unknown end-
 448 members, this variance can be increased to assess the composition.

449 Table 3: Mix calculation chemical composition of the end-members. Units expressed in mmol/L for
 450 chemical species and conservative components (*u*₁ and *u*₂) and mS/cm for EC.

	<i>u</i> ₁	<i>u</i> ₂	$\delta^{18}O$	δD	EC	<i>Br</i>	<i>Li</i>	<i>Cl</i>
Input end-members composition								
F1	6.972	7.210	-6.143	-37.527	0.980	0.011	0	1.881
SW	289.085	2.423	0.700	7.500	53.000	0.898	0.028	612.162
Output end-members composition								
F1_r	2.738	7.088	-5.92	-36.64	0.672	0.004	0	1.655
SW_r	287.983	1.262	0.684	6.627	56.894	0.883	0.012	552.43

451 The calculation also yields the proportion of each end-member in the observation wells
 452 using (Table 4). Results are grouped by the proportion of FW. Group A (more than 90% FW)
 453 includes all shallow piezometers, which is insistent with FW floating on top of SW. Group B
 454 (between 70 and 90% FW) includes most intermediate depth wells. Finally, the remaining
 455 samples are those of the deep and close to the shore piezometers. In summary, the observed
 456 general trend is a decrease of the FW fraction with depth and from inland to the coast.

457 Table 4 : Calculated fraction of FW in Argentona experimental site from EC, Cl^- water molecule
 458 isotopes and mixing calculations indicates wells located on the transect parallel to the coastline, **
 459 indicates fully screened wells.

Group	Wells	% F _{1r} in samples			
		EC	Cl	H ₂ O Isotopes	Mix code
A	N2-15	99.7	99.9	98.6	99.7
	*N4-15	99.4	99.6	98.5	99.6
	N3-15	98.8	99.1	93.9	97.4
	N1-15	96.1	96.6	89.0	93.7
	**PP15	93.9	95.0	90.2	92.7
B	N2-20	80.6	83.4	84.4	88.2
	*N4-20	63.2	68.2	75.4	78.3
	N3-20	76.7	80.2	82.4	85.9
	**PP20-A	72.7	76.8	75.2	77.8
C	N2-25	26.5	30.0	34.1	33.3
	*PS-25	13.1	20.7	25.9	24.5
	*N4-25	11.0	18.1	19.8	18.3
	N3-25	12.1	19.5	19.8	18.4
	N1-25	25.2	30.3	34.3	34.9
	N1-20	4.2	14.2	9.2	8.7
	**PP20-B	15.4	23.9	23.7	22.7

460

461 The contribution to the objective function (F_{Obj}) obtained by the MIX code after the
 462 mixing ratios end-members calculations are presented in Figure 4, classified by water sample
 463 (18), end-member (2), and chemical species (8). Note the largest contributions come from
 464 samples N1-15 (18%) and N3-15 (14%).

465 N1-15 is screened from 12.5 to 14.5 m, deeper than other boreholes belonging to the
 466 same group (Group A, Nx-15, from ~10 to 12 m). However, N1-15 is shallower than boreholes
 467 from Group B (Nx-20, from 15 to 17 m). Also, it is located just below a silt layer, identified at
 468 12 m by [Martínez-Pérez et al. \(2022\)](#). [Palacios et al. \(2020\)](#) presents this silt layer as a hydraulic
 469 barrier affecting the mixing zone dynamics. Despite this, N1-15 presents 93.7% of F_{1r} and a
 470 small SWr ratio that is reflecting a low penetration of the saltwater wedge at this sampling
 471 hydrologic condition.

472 MIX calculations for N3-15 pointed out a possible analytical error. $\delta^{18}O$ measured
473 concentration is higher (-5.475 ‰) than the calculated concentration (-5.745 ‰). This
474 calculated value is similar to another groundwater sampling campaign (-5.84 ‰), carried out
475 one month later in the same well and with the same hydrological conditions. $\delta^{18}O$ is the
476 chemical species with the highest contribution to the objective function and represents 35% of
477 F_{obj} (Figure 4). The rest of the species have a low contribution to the objective function. The
478 large contributions of stable isotopes to the objective function concentrate in the shallowest
479 (freshest) samples, suggests that the high variability of stable isotopes in rainfall and exchange
480 with surface water may not be well represented by a single freshwater end member.

		u1	u2	d18O	dD	EC	Br	Li	Cl	Total	Contribution to Fobj (%)
Normalized difference of end-members											
F1 vs F1r		-0.01	-0.08	-0.39	-0.14	-0.01	-0.02	-0.04	-0.01	-0.70	11.67
SW vs SWr		-0.12	0.00	0.00	-0.01	0.00	0.00	-0.16	-0.01	-0.29	4.87
Normalized difference of observation wells											
SEWAGE		0	0	0	0	0	0	0	0	0	0.00
RIVER		0	0	0	0	0	0	0	0	0	0.00
A	N2-15	-0.001	-0.003	-0.001	-0.125	-0.01	-0.013	-0.011	0	-0.164	2.74
	*N4-15	0	-0.005	-0.013	-0.14	-0.016	-0.015	-0.073	0	-0.263	4.39
	N3-15	0	-0.045	-0.575	-0.012	-0.039	-0.064	-0.008	-0.077	-0.82	13.69
	N1-15	-0.001	-0.097	-0.487	-0.149	-0.087	-0.076	-0.002	-0.187	-1.086	18.13
	**PP15	-0.001	-0.02	-0.125	0	-0.012	-0.007	-0.002	-0.042	-0.21	3.51
B	N2-20	-0.006	-0.052	-0.195	-0.076	-0.058	-0.051	-0.009	-0.064	-0.511	8.53
	*N4-20	-0.023	-0.056	-0.1	-0.037	-0.065	-0.053	-0.002	-0.073	-0.409	6.83
	N3-20	-0.01	-0.062	-0.1	-0.051	-0.059	-0.047	-0.055	-0.063	-0.446	7.44
	**PP20-A	-0.001	-0.004	-0.018	-0.019	-0.009	-0.003	-0.14	-0.009	-0.203	3.39
C	N2-25	-0.033	-0.005	-0.002	-0.007	0	-0.002	-0.049	-0.01	-0.109	1.82
	*PS-25	-0.071	0	-0.009	-0.019	-0.002	-0.002	-0.001	-0.01	-0.114	1.90
	*N4-25	-0.001	0	-0.006	-0.007	0	0	-0.026	-0.005	-0.045	0.75
	N3-25	-0.028	0	-0.006	-0.006	0	0	-0.019	-0.004	-0.063	1.05
	N1-25	-0.222	-0.005	-0.053	-0.023	-0.002	-0.003	-0.117	-0.012	-0.436	7.28
	N1-20	-0.064	0	0	-0.009	0	-0.001	-0.009	-0.001	-0.085	1.42
	**PP20-B	-0.028	0	-0.002	-0.002	0	0	0	-0.003	-0.036	0.60
Total		-0.619	-0.429	-2.081	-0.832	-0.373	-0.358	-0.726	-0.57	-5.991	
Contribution to Fobj (%)		10.33	7.16	34.74	13.89	6.23	5.98	12.12	9.51		

481
482
483
484

Figure 4: End-members and observation wells contribution to the objective function by species. Colored data bars are used to highlight the range of values, red colors to highlight observations maximum by species and grey is used for totals). A longer bar represents a higher value.

486 3.3.Step 3: Quantification of chemical reactions

487 Mixing calculations have been performed using components that, according to our
488 conceptual model, are conservative. We now use secondary species to calculate the extent of
489 chemical reactions (R_{rj} , Eq. 5) as the deviation between the measured and calculated by simple
490 mixing concentrations. The spatial distribution of R_{rj} expressed in mEq/L is presented in Figure
491 5 with positive (in red) and negative (in blue) values indicating the reaction direction, while
492 wheat color represents weak or no reaction. As a reference, Figure 5 displays the measured
493 electrical conductivity to identify the SWI distribution in the aquifer. Bear in mind that these
494 reaction amounts do not reflect the local reaction rate but the integrated reactions that have
495 occurred during GW transport since the end-member was sampled. As a result, one may
496 conjecture that the extents computed for the most saline (nearly SW) samples reflect reactions
497 that occurred shortly after sea water entered the aquifer.

498 Cation exchange reactions are the reactions with highest extent at the site. Specifically,
499 R2 presents the highest extent of all reactions (up to 60 mEq/L). This implies that a lot of Ca^{2+}
500 is desorbed to leave free sites for Na^+ . This reaction is identified throughout the aquifer but
501 probably occurs immediately after SW enters in contact with exchange sites. In fact, the extent
502 of cation exchange (Na-Ca) is small in the inland and shallow part of the aquifer, where the
503 fraction of SW is small. Note, however, that highest Na^+ sorption does not occur at the most
504 saline sample, but at the deepest part of the aquifer, in the seawater intrusion front, which we
505 attribute to either kinetic control (the deepest samples are probably the oldest ones), to transport
506 across weathered granite at the base of the aquifer, or to transient fluctuations of the SW front
507 (see discussion for Magnesium below).

508 R3 displays lower extent values than R2, and a maximum of 6 mEq/L of K^+ is
509 exchanged with Ca^{2+} . This reaction is also found mainly in the salty part of the aquifer (> 45

510 mS/cm). The last cation exchange reaction considered is Mg – Ca exchange (R4), which is
511 found in the two directions, with some Mg^{2+} sorption ($R > 0$) up to 5.5 mEq/L and a strong
512 desorption ($R < 0$) up to 30 mEq/L. Changes in magnesium concentration can only be attributed
513 to sorption/desorption reactions as the Mg-rich minerals at the site, are a Mg-rich-hornblende
514 and some biotite identified as trace and could not explain up to 30 mEq/L excess of Mg^{2+} by
515 dissolution processes. Strong magnesium desorption is somewhat unexpected as $[Mg^{2+}]$ is
516 already high in seawater. Mg^{2+} desorption occurs in the deep and middle aquifer portion in the
517 inland part. At this same level, we observe the highest Na^+ sorption values. Accordingly, we
518 attribute the desorption of Mg^{2+} to transient exchange with Na^+ . That is, Mg^{2+} that was sorbed
519 in a previous freshening event may be desorbed when the SW front advances. In fact, salty
520 samples often display more magnesium than would be expected from seawater (Kouzana et al.,
521 2009; Mahlnecht et al., 2017; Shin et al., 2020). The release of chemical elements can be
522 directly correlated with the ionic strength of the solution and the selectivity of a material for
523 certain cations. Jiao and Post (2019) defined the selectivity sequence as $Na^+ > K^+ > Mg^{2+} >$
524 Ca^{2+} , which coincides with the cation exchange sequence observed in Argenton. Na^+ sorption
525 in the front of the SWI, followed by the K^+ in the salty part and the desorption of the Mg^{2+} a
526 posteriori. Still, the most salient feature is the high sensitivity to salinity, which coupled to
527 transient fluctuations explains anomalously high values of Mg^{2+} and Ca^{2+} .

528 R_1 displays positive values indicating that the release of calcium promotes the
529 precipitation of gypsum. The large quantity of Ca^{2+} released during SW penetration, together
530 with the high SO_4^{2-} in seawater (2907 mg/L) promotes the precipitation of gypsum. In this
531 way, the area where gypsum will precipitate the most will be the area where Ca^{2+} is released,
532 which explains why gypsum precipitation patterns are similar to Ca^{2+} desorption patterns. We
533 observe that FW boreholes exhibit values close to 0 mEq/L of gypsum precipitation. This
534 observation is in good agreement with Gomis-Yagües et al. (2000) that demonstrated the

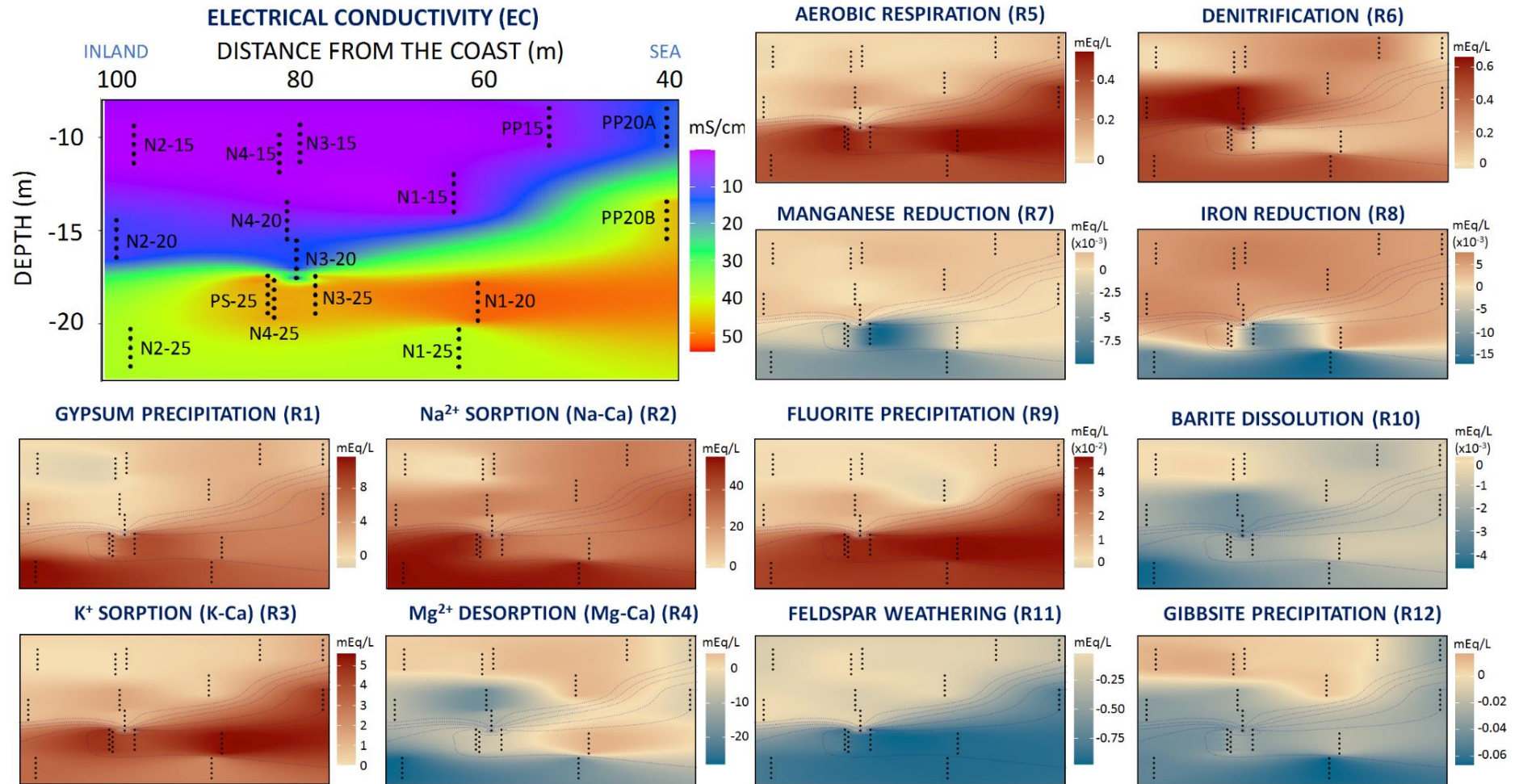
535 possibility of gypsum precipitation at the salinity front during seawater intrusion. Note that
536 some sulfate concentration abatement could also be attributed to sulfate-reduction as mentioned
537 by [Canfield \(2001\)](#), a possibility we have not explored here.

538 For the discussion of redox reaction amounts, it is important to recall that Figure 5
539 should not be interpreted as a map of the place where reactions take place, but of the reaction
540 amounts required to explain the observed chemistry. Actual reactions may have occurred
541 anywhere along the way. The values associated to aerobic respiration reflect that we assume
542 SW to be initially fully oxygenated (~ 10 mg/l) as it is in equilibrium with the atmosphere while
543 freshwater dissolved oxygen is reduced due to aerobic reactions in the aquifer. We measured
544 low DO in deep boreholes (ranging from 0.1 to 1.5 mg/l) such as in PS25 and N4-25 which
545 imply that aerobic respiration (R5, Figure 5) has occurred. Nevertheless, we consider that this
546 reaction is probably not occurring in these boreholes but near the seafloor where organic matter
547 from dead marine biota is usually available.

548 Denitrification is also occurring as $R6 > 0$ (Figure 5). The reaction is mainly localized
549 in the middle and deep part of the aquifer section (Nx-20 and Nx-25 level). Unlike R5, where
550 oxygen comes from the sea, nitrate in R6 comes from FW, which explains why denitrification
551 is most apparent in the mixing zone. Mn reduction (R7) and Fe reduction (R8) display similar
552 patterns, with small reaction extents. Here, negative values indicate that Mn^{2+} and Fe^{2+} are
553 released to groundwater (probably reflecting reduction of ferric oxydes or dissolution of pyrite).
554 This occurs only in the deepest part of the aquifer, where O_2 is absent. Elsewhere, Mn and Fe
555 are oxidized. However, it appears that N3-25 stands out from other boreholes located at the
556 same depth. It forms a localized zone with reducing conditions, which has been observed by
557 various studies on other places ([Brown et al., 1999](#); [Chapelle & Lovley, 1992](#)). For this well, a
558 higher proportion of clay was measured and a slower response to tidal fluctuations ([Martínez-](#)

559 [Pérez et al., 2022](#)). This may favor redox reactions due to lower groundwater circulation and/or
560 higher concentrations of iron oxides. In all, Mn^{2+} and Fe^{2+} appear to be mobilized during
561 intrusion but oxidized and precipitated in the mixing zone.

562 Finally, R9 to R10 are dissolution-precipitation processes or weathering of minerals.
563 Fluorite dissolution-precipitation is driven by the Calcium released by cation exchange.
564 Therefore, it is virtually absent in the FW portion and highest where calcium is highest. Both
565 R10 and R11, display negative values which indicate mineral dissolution. Barite dissolution
566 (R10) is very low (max 0.0046 mEq/L) and does not show a specific pattern. In the freshwater
567 part of the aquifer, *R* presents higher values (boreholes N2-15, N3-15, and N4-15). Feldspar
568 weathering (R11) is following the SWI shape with more alteration near the coast and increasing
569 with depth (up to 1 mEq/L). Note that the granite is less weathered at depth, and, thus, ready
570 for further alteration. As a consequence of feldspar alteration, Al tends to precipitate in the same
571 areas and in these pH conditions (pH>5, which destabilizes aluminum). We quantify Al
572 precipitation as gibbsite precipitation (R12) which is consistent with pH variability. Still, some
573 clay precipitation might also act as an Al sink.



574

575

576

577

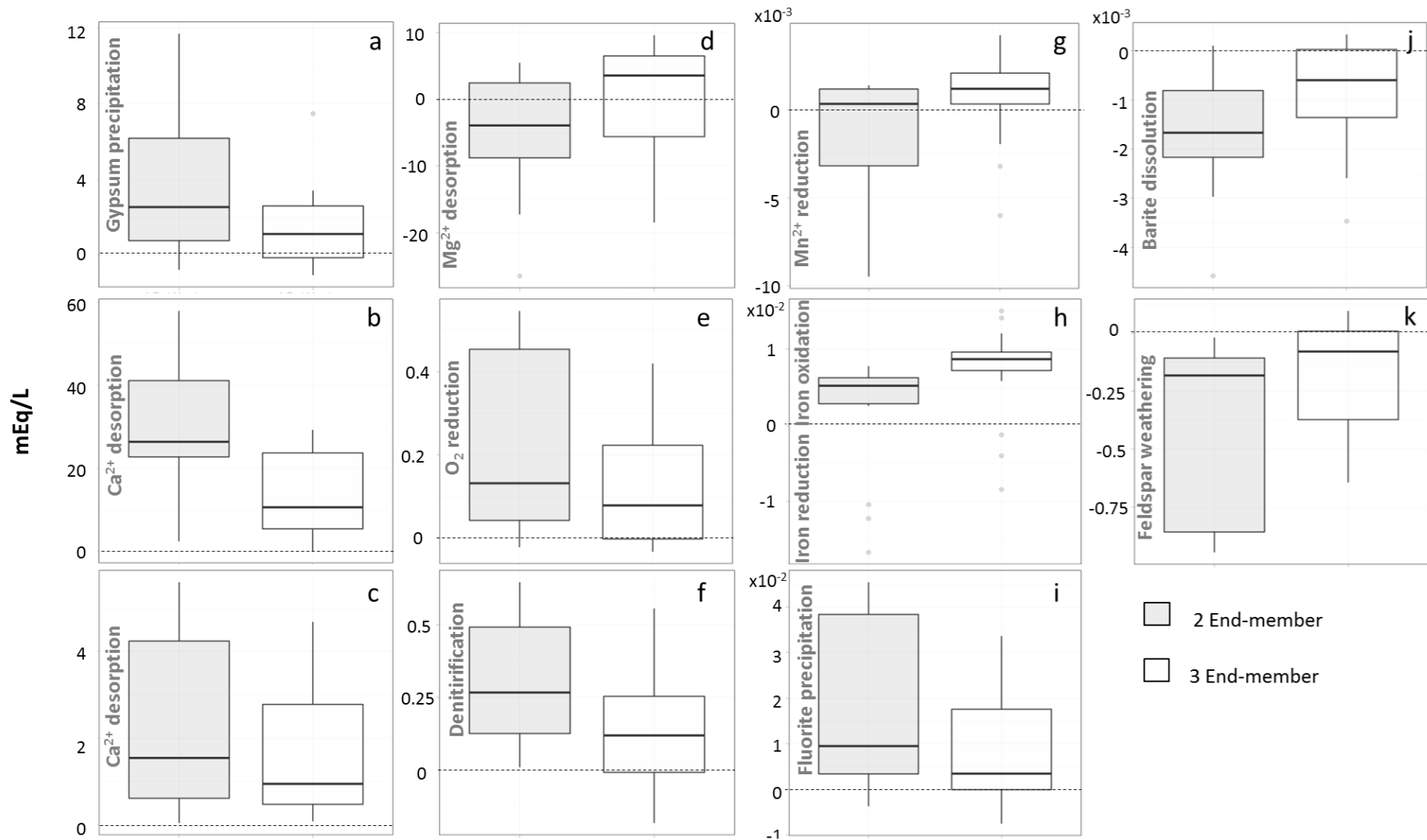
Figure 5: Chemical reaction amounts at the site samples. Note that the maps do not represent where the reactions take place, but the amount (mEq/L) needed to explain the observed concentrations. EC is displayed in the upper left as a SWI reference and dotted lines represent EC contours (15, 20, 25, 35, 45 mS/cm) in other subfigures.

578 **3.4. Two end-members vs Three end-members accuracy**

579 As presented in Section 3.1, the EMMA requires 3 end-members (Figure 3l) to explain
580 97.55% of the variance in iteration 3. Figure 6 presents a comparison between the reaction
581 extent using 2 end-members (as presented in Figure 5) and 3 end-members (F1, SW, and N1-
582 25, Figure 3l). We observe that, for most reactions, the reaction extent is reduced with respect
583 to the case with 2 end-members. An average of 49% less gypsum (Figure 6a) and fluorite
584 (Figure 6i) precipitate because calcium desorption (R2 to R4, Figure 6b, c, d) is reduced by an
585 average of 31%. This is related to the 3rd end-member composition (recalculated based on N1-
586 25 concentrations), which contributes with more Mg and less Na than seawater. Therefore, no
587 competition between Na and Mg for exchange sites occurs, avoiding Mg desorption as it was
588 occurring with 2 end-members (Figure 6d). The reductions of dissolved oxygen (Figure 6e) and
589 denitrification (Figure 6f) are much lower (46% and 30% less) because they are already low in
590 the 3rd end-member. So that the concentration reduction is caused by dilution instead redox
591 reactions. We observe that using 3 end-members can lead to the opposite reaction as for R6
592 where negative R values are observed. With 2 end-members, Mn and Fe reduction (R7 and R8)
593 were only affecting the deepest wells, and to a lesser extent Mn reduction was occurring at
594 intermediate depths (Nx-20). However, if we consider three end-members, this manganese
595 reduction is not observed and both Mn and Fe reduction are lower (40 and 50% less
596 respectively). In the same way, considering a third end-member the barite dissolution and
597 feldspar weathering are reduced by 37% and 57% respectively since the chemical compounds
598 such as SO₄, Ba, Si, and Al are modified by mixing processes. In conclusion, adding a third
599 end-member minimizes the occurrence of chemical reactions.

600 These results illustrate the nature of our calculations. Computed reactions amounts
601 reflect what is needed to explain derivations from mixing calculations. If an end-member has
602 already suffered some reactions, the corresponding extents will implicitly accounted for by this

603 end member. In our case, both the 2 and 3 end-members models are valid representations of the
604 chemical system. But we prefer the 2 member calculation for parsimony, because it represents
605 two true end members (the third one is really a reacted mixture of the other two), and because
606 it represents better the actual reaction extents.



607

608 Figure 6: Comparison of reactions extent considering 2 end-members (gray) and 3 end-members (white)

609 **3.5.Implications for SGD**

610 It is well known that nutrients and pollutants are delivered into the coastal zone
611 through SGD via submarine springs and seeps (B. Burnett, 1999; William C. Burnett,
612 1996; William C. Burnett et al., 2001; Monastersky, 1996). Yet, SGD contribution is often
613 ignored for the assessment of biogeochemical cycles at the sea, mostly due to the lack of
614 chemical data (Duque et al., 2020). Indeed, SGD samplings are difficult, except in karst
615 environments, where the high flow rate of the submarine springs facilitate identification
616 and sampling (Fleury et al., 2007). Elsewhere, SGD tend to be diffuse, which hinders
617 sampling. This is especially true in alluvial aquifers and further complicated the spatio-
618 temporal fluctuations of the discharge. Our method could address the limitations of direct
619 sampling by determining how chemical reactions in the change the composition of SW
620 and the easy to sample FW. The application to the Argenton site illustrates the high
621 reactivity that can be found in coastal aquifers. It is worth stressing that we have identified
622 reactions that occur to the three types of SGD: FW (Group A), mixed (Group B) and
623 recirculated SW (Group C). FW is easy to characterise by direct sampling. We were not
624 surprised by the high reactivity of the mixing zone, which is expected to result from
625 mixing two widely different waters (e.g., Wigley and Plummer, 1976; Rezaei et al., 2005).
626 In hindsight, we should also have expected a high reactivity in the recirculated SW zone
627 to result from SW-rock interactions.

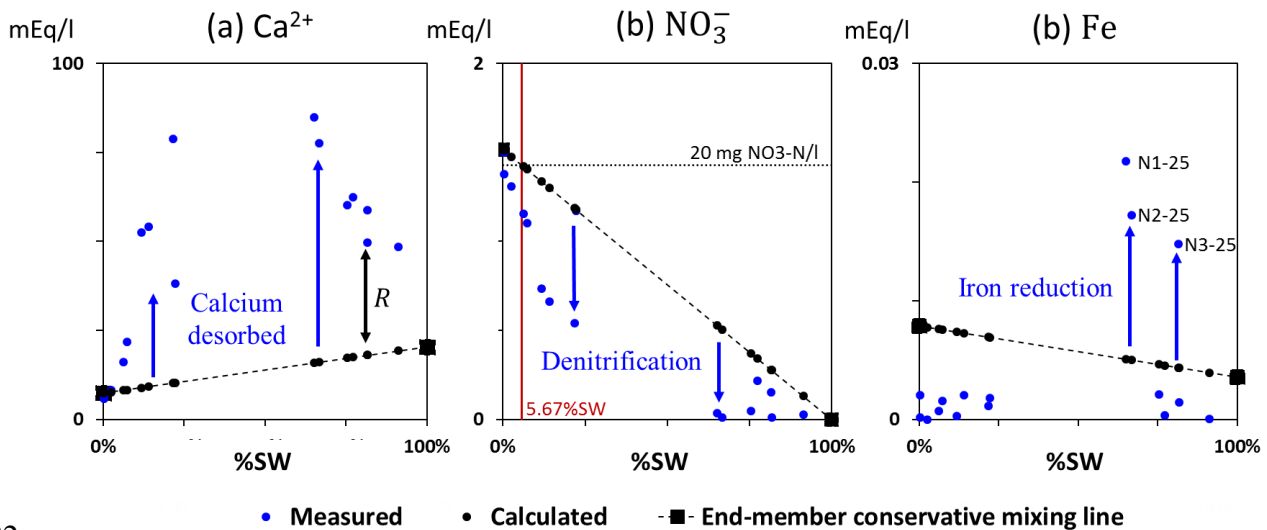
628 For example, as mentioned previously, the simple mixing of end-members cannot
629 explain the Ca^{2+} concentrations sampled in coastal aquifers since much more calcium is
630 measured (Figure 7). At the Argenton experimental site, measured Ca^{2+} concentrations
631 can reach 4 times the concentration measured in seawater. We attributed this
632 concentration to desorption processes (i.e. cation exchange), attenuated by some gypsum
633 and fluoride precipitation limiting Ca^{2+} concentration increase. We estimated that the

634 ratio of Ca^{2+} desorption-precipitation decreases from inland to the sea in groups B and C
635 (Table 4.5), with an average of $8\% \pm 4\%$ and $19\% \pm 8\%$ respectively. This confirms that
636 calcium will build up in SW immediately upon entrance in the aquifer. Ca^{2+} concentration
637 in the sea is not very high (some 400 mg / L) and the oversaturation in calcite and other
638 carbonate minerals means that the availability of Ca^{2+} is usually not a limiting element
639 for the biological activity ([Morse & Berner, 1995](#)). Still, in laggons and/or closed areas,
640 the calcium discharge can affect the carbonates balance. For example, [Gattuso et al.](#)
641 [\(1998\)](#) demonstrated that coral calcification increases nearly 3-fold when aragonite
642 saturation increases from 98% to 390%. Yet, the SW pH reduction associated to
643 anthropogenic release of CO_2 into the atmosphere is reducing carbonate concentration
644 and the saturation states of biologically important calcium carbonate minerals ([Barker &](#)
645 [Ridgwell, 2012](#)). Increased atmospheric CO_2 is making Ca^{2+} inflows critical.

646 Nitrogen is a limiting element for photosynthetic organisms (plants or algae) in
647 most oceans ($\sim 75\%$, [Bristow et al., 2017](#)). The N cycle has been dramatically altered by
648 industrially fixed nitrogen by humans and wastewater discharge. We have seen that the
649 aquifer plays an important role in the reduction of nitrates, through denitrification.
650 Problems may appear when the nitrate rich FW discharges into the sea and denitrification
651 is not sufficient to eliminate the nitrate overload, which may cause local eutrophication.
652 No safe level of nitrate has been established for aquatic animals ([Scott & Crunkilton,](#)
653 [2000](#); [U. S. Environmental Protection Agency, 1986](#)). The only existing limitation is for
654 seawater culture with a maximum concentration of 20 mg $\text{NO}_3\text{-N}$ / l ([Spotte \(1979\)](#),
655 indicated by a dotted line on Figure 7b). In the case of Argenton, if there were no
656 reactions and nitrate concentration would be reduced by dilution only, this limit would be
657 exceeded at all the shallow wells (N2-15, N3-15, and N4-15) where there is less than 5%
658 SW, which may be cause eutrophication in closed lagoons (e.g., [Velasco et al., 2006](#)). But

659 denitrification reduces significantly nitrate concentrations (Figure 7), a limiting nutrient
660 in oligotrophic seas. In either, denitrification is relevant.

661 Finally, seawater is characterized by low Fe (below 0.5 nM, Liu and Millero,
662 2002) because it tends to precipitate under aerobic conditions, so that river inflow is
663 restricted to iron suspended particles. Yet, iron is an oligoelement that limits primary
664 production in large portions of the ocean. For example, Fe loading from SGD has been
665 shown to stimulate primary production in the South Atlantic Ocean ([Windom et al.,](#)
666 [2006](#)). Fe requires reducing conditions to promote Fe mobility. The highest
667 concentrations were measured in N1-25, N2-25 and N3-25 (0.61, 0.48 and 0.41 mg/L
668 respectively), where we identified the highest iron reduction. Not surprisingly, these wells
669 are deep and depleted in oxygen and nitrates, which has also been observed in Indonesia
670 ([Rusydi et al., 2021](#)). In the rest of the wells, we observe that the concentrations are much
671 lower than the conservative mixing line. Since our measurement of Fe in SW is
672 anomalously high, we place little emphasis on Fe depletion in the saline portion. Instead,
673 it is clear that some iron has been mobilized in the saline portion of the aquifer, and that
674 this iron has been removed upon mixing with FW, which probably reflects oxidation and
675 precipitation. A very similar comment can be made about Mn, which is “linked to nearly
676 all other elemental cycles and intricately involved in the health, metabolism and function
677 of the ocean's microbiome” (Hansel, 2017) and displays very low concentrations in SW
678 (less than 1 ppb, van Hulst et al., 2016). In short, both Fe and Mn may display significant
679 concentrations in SW recirculated SGD, but probably not FW or mixed SGD. The fact
680 that both elements are relatively abundant in the crust leads us to conjecture that SGD
681 may be a significant source of Fe and Mn into the ocean.



682

683 Figure 7: Production or loss of key elements (a: Ca^{2+} ; b: NO_3^- ; c: Fe) to SGD as a consequence of
 684 geochemical reactions induced by mixing between FW and SW

4. Conclusion

685

End Member Mixing Analysis (EMMA), which has been traditionally associated
 686 to the calculation of mixing ratios, is a promising tool to identify and quantify
 687 hydrochemical processes occurring in both coastal and inland aquifers. In this work, we
 688 described a detailed methodology to do so, and applied it to an alluvial coastal aquifer
 689 (Argentona experimental site). We have deduced chemical reactions in the fresh, saline,
 690 and mixing zone groundwater samples.

691

The complexity and high activity of coastal aquifers makes interpretation of
 692 groundwater chemistry difficult. Application of the proposed reactive EMMA has
 693 facilitated this task. Reactive EMMA reduces the dimension of the chemical system by
 694 the use of conservative components instead of reactive chemical species, but removes the
 695 dispersion caused by chemical reactions. At the Argentona site, this led to an increase of
 696 the EMMA performance (reaching up to 97% of the variance explained by a single
 697 eigenvalue, i.e., two end-members). This has facilitated computation of mixing ratios and
 698 led to an overall robust performance. This easy methodology can be extended and

699 strongly recommended to other aquifers to understand processes taking place in each
700 geological/hydrogeological context (affecting compound released to the sea by SGD) and
701 also include it in temporal monitoring (i.e., progradation of carbonate dissolution in
702 karstic systems, trace contaminants discharge/retention and sources).

703 The EMMA has allowed us not only to obtain a consistent and simple
704 identification of end-members, but also to identify chemical reactions and to quantify
705 their extent. Chemical reaction identification and quantification for each sample
706 facilitates representing and understanding the spatial distribution of chemical processes
707 within the aquifer. Quantifying the reactions and where they occur allows not only to
708 know in which elements will SGD be enriched, but also to identify the composition of
709 each type of SGD (FW outflow, SW recirculation, or mixed FW and SW).

710 We found that the highest reaction extent corresponds to cation exchange (up to
711 60 mEq of Ca^{2+} exchanged with Na^+). Calcium is a good example of the interdependence
712 of chemical reactions (involved directly or indirectly in 7 chemical reactions in our
713 system). This indicates that at least 8 species would have been removed from the chemical
714 system if we had adopted the traditional EMMA (only conservative species). On the other
715 extreme, we deduced other reactions, such as feldspar weathering or gibbsite
716 precipitation, which are probably more specific to our site but still relevant to understand
717 the origin of our samples and the processes undergone by GW.

718 While our quantitative results are site specific, we conjecture that many can be
719 expected elsewhere. Specifically, reducing conditions should be expected below the
720 seabed virtually everywhere due to dead biota. This will favor the mobilization of Fe and
721 Mn, which are important for ocean biochemical cycles. Cation exchange is ubiquitous
722 and should be expected in most places.

Supplementary materials

723

A. Hydrochemical data for EMMA analysis

n_s	1	2	3	4	5	6	7	8	9	10	11	12	13	14	15	16	17	18	19	20
Chemical species	Alk	Al	Ca	SO4	Na	K	Mg	DO	NO3	Mn	Fe	F	Ba	Si	d18O	dD	EC	Br	Li	Cl
Units	mmol/L	mmol/L	mmol/L	mmol/L	mmol/L	mmol/L	mmol/L	mmol/L	mmol/L	mmol/L	mmol/L	mmol/L	mmol/L	mmol/L	‰	‰	mS/cm	mmol/L	mmol/L	mmol/L
F1	5.279	0.005	3.668	1.072	4.703	0.064	1.943	0.035	1.516	0.001	0.004	0.010	0.000	0.329	-6.143	-37.527	0.980	0.011	0.000	1.881
SW	2.098	0.008	10.233	30.259	489.071	9.890	59.659	0.324	0.000	0.000	0.002	0.057	0.000	0.004	0.700	7.500	53.000	0.898	0.028	612.162
N1-25	1.901	0.030	42.429	16.037	265.893	3.916	48.146	0.025	0.037	0.004	0.011	0.004	0.001	0.354	-1.700	-8.100	39.900	0.621	0.016	427.055
SEWAGE	4.918	0.000	0.158	0.015	0.110	0.009	0.016	0.032	0.006	0.000	0.001	0.001	0.000	0.285	-6.185	-37.804	0.600	0.000	0.000	0.047
RIVER	4.918	0.000	0.818	0.068	0.482	0.345	0.582	0.032	0.105	0.000	0.018	0.004	0.003	0.285	-6.154	-37.599	0.880	0.000	0.000	0.241
PP15	4.902	0.006	10.882	1.837	11.733	0.146	4.616	0.036	1.102	0.000	0.001	0.009	0.001	0.336	-5.310	-33.522	4.140	0.061	0.001	32.558
PP20A	4.602	0.017	19.060	6.929	87.109	0.720	16.297	0.047	1.171	0.000	0.001	0.014	0.001	0.313	-4.500	-26.700	15.190	0.215	0.001	143.759
N1-15	5.502	0.003	8.067	1.714	9.757	0.134	3.120	0.022	1.154	0.000	0.000	0.017	0.001	0.330	-5.252	-32.992	2.990	0.043	0.001	22.537
N3-15	5.102	0.003	4.108	1.462	5.414	0.145	1.535	0.028	1.310	0.000	0.000	0.013	0.000	0.338	-5.475	-35.235	1.580	0.015	0.001	7.210
N4-15	5.502	0.001	3.317	1.561	4.125	0.049	1.121	0.007	1.379	0.000	0.000	0.010	0.000	0.332	-5.933	-37.330	1.290	0.013	0.001	4.042
N2-15	4.802	0.000	2.921	1.480	3.661	0.050	0.979	0.046	1.500	0.000	0.001	0.012	0.000	0.360	-5.890	-37.350	1.120	0.012	0.000	2.499
PP20B	3.101	0.019	31.176	20.956	338.865	2.950	48.337	0.016	0.219	0.000	0.000	0.009	0.001	0.272	-0.800	-3.300	45.000	0.680	0.009	466.107
N1-20	2.701	0.016	24.268	24.768	420.467	3.437	51.880	0.025	0.027	0.001	0.000	0.008	0.001	0.268	0.100	3.300	50.800	0.768	0.010	525.340
N3-20	4.602	0.016	27.094	4.783	57.205	0.431	15.226	0.053	0.663	0.000	0.001	0.009	0.002	0.311	-5.100	-30.000	13.090	0.184	0.001	122.992
N4-20	4.101	0.015	39.368	7.255	83.429	0.634	23.050	0.016	0.539	0.001	0.001	0.009	0.002	0.292	-4.600	-26.800	20.100	0.288	0.003	195.685
N2-20	4.802	0.018	26.207	3.607	35.699	0.336	12.883	0.053	0.734	0.000	0.000	0.011	0.001	0.299	-5.300	-30.900	11.080	0.158	0.001	103.385
N3-25	2.801	0.019	24.821	20.760	366.816	3.914	51.161	0.048	0.155	0.005	0.007	0.008	0.001	0.298	-0.500	-1.500	46.700	0.723	0.012	493.298
N4-25	2.401	0.016	29.363	21.385	356.742	3.636	52.437	0.014	0.010	0.002	0.001	0.007	0.001	0.287	-0.500	-1.500	47.300	0.734	0.013	502.001
N2-25	2.501	0.024	38.779	14.683	269.921	3.267	53.693	0.032	0.010	0.003	0.009	0.006	0.002	0.323	-1.500	-8.000	39.200	0.628	0.012	428.945
PS25	1.891	0.022	30.061	21.048	320.761	2.628	48.101	0.003	0.046	0.002	0.001	0.007	0.001	0.279	-0.900	-4.300	46.200	0.710	0.010	485.614

725

726 **B. Iteration 1: Stoichiometric and component matrix for cation exchange and**
 727 **gypsum precipitation**

728 We start from a chemical system governed by four chemical reactions ($n_r = 4$),
 729 with cation exchange (Na-Ca, K-Ca and Mg-Ca) and gypsum precipitation. We defined
 730 SO_4 , Na, K and Mg as secondary species. Such that the stoichiometric matrix can be
 731 written as: $S = (S_1|-I)$. The secondary species have to coincides with the opposite of the
 732 identity matrix, I . For this first chemical system the stoichiometric matrix is:|

Stoichiometric matrix		1	2	3	4	5	6	7	8	9	10	11	12	13	14
		Alk	Al	Ca	DO	NO3	Mn	Fe	F	Ba	Si	SO4	Na	K	Mg
R1	Ca - yeso = SO4	R1	0	0	-1	0	0	0	0	0	0	-1	0	0	0
R2	Na + 0.5X-Ca =X-Na + 0.5Ca	R2	0	0	0.5	0	0	0	0	0	0	0	-1	0	0
R3	K + 0.5X-Ca =X-K + 0.5Ca	R3	0	0	0.5	0	0	0	0	0	0	0	0	-1	0
R4	Mg + X-Ca = Ca - X-Mg	R4	0	0	1	0	0	0	0	0	0	0	0	0	-1

Primary species Secondary species

733

734 The component matrix (U) is then obtained by transforming the stoichiometric matrix as
 735 follows $U = (I|S_u^t)$. The obtained component matrix for iteration 1 is:

Components matrix		Alk	Al	Ca	DO	NO3	Mn	Fe	F	Ba	Si	SO4	Na	K	Mg
	Alk	1	0	0	0	0	0	0	0	0	0	0	0	0	0
	Al	0	1	0	0	0	0	0	0	0	0	0	0	0	0
u1	Ca-SO4+0.5Na+0.5K+Mg	0	0	1	0	0	0	0	0	0	0	-1	0.5	0.5	1
	DO	0	0	0	1	0	0	0	0	0	0	0	0	0	0
	NO3	0	0	0	0	1	0	0	0	0	0	0	0	0	0
	Mn	0	0	0	0	0	1	0	0	0	0	0	0	0	0
	Fe	0	0	0	0	0	0	1	0	0	0	0	0	0	0
	F	0	0	0	0	0	0	0	1	0	0	0	0	0	0
	Ba	0	0	0	0	0	0	0	0	1	0	0	0	0	0
	Si	0	0	0	0	0	0	0	0	0	1	0	0	0	0

736

737 In this first iteration, one conservative component is obtained such that: $u_1 = Ca^{2+} -$
 738 $SO_4^{2-} + 0.5Na^+ + 0.5K^+ + Mg^{2+}$. Then the same process is repeated for each chemical
 739 system, where new chemical reactions are included in the stoichiometric matrix.

740 **C. Iteration 2: Stoichiometric and component matrix for redox reactions**

741 The stoichiometric matrix is:

		1	2	3	4	5	6	7	8	9	10	11	12	13	14
Stoichiometric matrix		Alk	Al	Ca	F	Ba	Si	SO4	Na	K	Mg	DO	NO3	Mn	Fe
R1	Ca - yeso = SO4	R1	0	0	-1	0	0	0	-1	0	0	0	0	0	0
R2	Na + 0.5X-Ca =X-Na + 0.5Ca	R2	0	0	0.5	0	0	0	0	-1	0	0	0	0	0
R3	K + 0.5X-Ca =X-K + 0.5Ca	R3	0	0	0.5	0	0	0	0	0	-1	0	0	0	0
R4	Mg + X-Ca = Ca - X-Mg	R4	0	0	1	0	0	0	0	0	0	-1	0	0	0
R5	Redox O2	R5	1	0	0	0	0	0	0	0	0	0	-1	0	0
R6	Redox NO3	R6	1.25	0	0	0	0	0	0	0	0	0	0	-1	0
R7	Redox Mn	R7	0.5	0	0	0	0	0	0	0	0	0	0	0	-1
R8	Redox Fe	R8	0.25	0	0	0	0	0	0	0	0	0	0	0	0

Primary species Secondary species

742

743 The component matrix is:

		Alk	Al	Ca	F	Ba	Si	SO4	Na	K	Mg	DO	NO3	Mn	Fe
u2	Alk + DO + 1.25NO3 + 0.5Mn + 0.25Fe	1	1	0	0	0	0	0	0	0	0	1	1.25	0.5	0.25
	Al	2	0	1	0	0	0	0	0	0	0	0	0	0	0
u1	Ca - SO4 + 0.5Na + 0.5K + Mg	3	0	0	1	0	0	0	-1	0.5	0.5	1	0	0	0
	F	4	0	0	0	1	0	0	0	0	0	0	0	0	0
	Ba	5	0	0	0	0	1	0	0	0	0	0	0	0	0
	Si	6	0	0	0	0	0	1	0	0	0	0	0	0	0

744

745 A new conservative component is obtained : $u_2 = HCO_3^- + DO + 1.25NO_3^- +$
 746 $0.5Mn^{2+} + 0.25Fe^{2+}$.

747 **D. Iteration 3: Stoichiometric and component matrix for minerals dissolution-**
 748 **precipitation reactions**

749 The stoichiometric matrix is:

		1	2	3	4	5	6	7	8	9	10	11	12	13	14
Stoichiometric matrix		Alk	Al	Ca	SO4	Na	K	Mg	DO	NO3	Mn	Fe	F	Ba	Si
R1	Ca - yeso = SO4	R1	0	0	-1	0	0	0	0	0	0	0	0	0	0
R2	Na + 0.5X-Ca =X-Na + 0.5Ca	R2	0	0	0.5	0	-1	0	0	0	0	0	0	0	0
R3	K + 0.5X-Ca =X-K + 0.5Ca	R3	0	0	0.5	0	0	-1	0	0	0	0	0	0	0
R4	Mg + X-Ca = Ca - X-Mg	R4	0	0	1	0	0	0	-1	0	0	0	0	0	0
R5	Redox O2	R5	1	0	0	0	0	0	0	-1	0	0	0	0	0
R6	Redox NO3	R6	1.25	0	0	0	0	0	0	0	-1	0	0	0	0
R7	Redox Mn	R7	0.5	0	0	0	0	0	0	0	0	-1	0	0	0
R8	Redox Fe	R8	0.25	0	0	0	0	0	0	0	0	0	-1	0	0
R9	F + 1/2Ca = 1/2CaF2	R9	0	0	-0.5	0	0	0	0	0	0	0	0	-1	0
R10	Ba + SO4 = BaSO4	R10	0	0	1	0	0	0	0	0	0	0	0	0	-1
R11	Si = 1/3Feldspath Alteration - 1/3K - 1/3 Al	R11	0	0.33	0.17	0	0	0	0	0	0	0	0	0	-1

Primary species Secondary species

750

751 The component matrix is:

		Alk	Al	Ca	SO4	Na	K	Mg	DO	NO3	Mn	Fe	F	Ba	Si
u2	Alk + DO + 1.25NO3 + 0.5Mn + 0.25Fe	1	1	0	0	0	0	0	1	1.25	0.5	0.25	0	0	0
u3	Al + 0.33 Si	2	0	1	0	0	0	0	0	0	0	0	0	0	0.33
u1	Ca - SO4 + 0.5Na + 0.5K + Mg - 0.5F + Ba + 1/6Si	3	0	0	1	-1	0.5	0.5	1	0	0	0	0	-0.5	1

752

753 A new conservative component is obtained : $u_3 = Al^{3+} + 1/3Si^{4+}$ and the
 754 conservatives components u_1 and u_2 now reads as follows: $u_1 = Ca^{2+} - SO_4^{2-} +$
 755 $0.5Na^+ + 0.5K^+ + Mg^{2+} - 0.5F^- + Ba^{2+} + 1/6Si^{4+}$. u_2 is identical to the previous
 756 iteration: $u_2 = HCO_3^- + DO + 1.25NO_3^- + 0.5Mn^{2+} + 0.25Fe^{2+}$.

757 **E. Iteration 4: Stoichiometric and component matrix for gibbsite precipitation**

758 The stoichiometric matrix is:

	1	2	3	4	5	6	7	8	9	10	11	12	13	14
	Alk	Ca	SO4	Na	K	Mg	DO	NO3	Mn	Fe	F	Ba	Si	Al
Stoichiometric matrix														
Ca - yeso = SO4	R1	0	-1	-1	0	0	0	0	0	0	0	0	0	0
Na + 0.5X-Ca =X-Na + 0.5Ca	R2	0	0.5	0	-1	0	0	0	0	0	0	0	0	0
K + 0.5X-Ca =X-K + 0.5Ca	R3	0	0.5	0	0	-1	0	0	0	0	0	0	0	0
Mg + X-Ca = Ca - X-Mg	R4	0	1	0	0	0	-1	0	0	0	0	0	0	0
Redox O2	R5	1	0	0	0	0	0	-1	0	0	0	0	0	0
Redox NO3	R6	1.25	0	0	0	0	0	0	-1	0	0	0	0	0
Redox Mn	R7	0.5	0	0	0	0	0	0	0	-1	0	0	0	0
Redox Fe	R8	0.25	0	0	0	0	0	0	0	0	-1	0	0	0
F + 1/2Ca = 1/2CaF3	R9	0	-0.5	0	0	0	0	0	0	0	0	-1	0	0
Ba + SO4 = BaSO4	R10	0	1	0	0	0	0	0	0	0	0	0	-1	0
Si = 1/3Feldspath Alteration - 1/3K - 1/3 Al	R11	0	0.17	0	0	0	0	0	0	0	0	0	0	-1
Al --> Gibbsite	R12	0	0	0	0	0	0	0	0	0	0	0	0	-1

759

760 The component matrix is:

	Alk	Ca	SO4	Na	K	Mg	DO	NO3	Mn	Fe	F	Ba	Si	Al
u2 Alk + DO +1.25NO3 + 0.5Mn + 0.25Fe	1	1	0	0	0	0	1	1.25	0.5	0.25	0	0	0	0
u1 Ca - SO4 + 0.5Na + 0.5K + Mg -0.5F + Ba + 1/6Si	2	0	1	-1	0.5	0.5	1	0	0	0	-0.5	1	0.17	0

761

762 During this iteration, u_3 is removed and only the conservative components u_1 and
 763 u_2 remain unchanged.

764

Acknowledgements:

765 This work has been funded by the Spanish Government through MEDISTRAES
 766 III projects (grant nos. PID2019-110212RB-C22 and PID2019-110311RB-C21), LOGIC
 767 project (grant no. RTC2019-007484-5) and IDAEA-CSIC Center of Excellence Severo
 768 Ochoa (Grant CEX2018-000794-S). This work is also part of the project TerraMar (grant
 769 no. ACA210/18/00007) of the Catalan Water Agency. We also acknowledge the Spanish
 770 Ministry of Economy, Industry and Competitiveness for the PhD fellowship (BES-2017-
 771 080028) from the FPI Program awarded to T. Goyetche. The author A. Folch is a Serra
 772 Hünter Fellow.

Bibliography

773 Alfarrach, N., & Walraevens, K. (2018). Groundwater overexploitation and seawater
 774 intrusion in coastal areas of arid and semi-arid regions. *Water*, 10(2), 143.
 775 Andersen, M. S., Nyvang, V., Jakobsen, R., & Postma, D. (2005). Geochemical processes
 776 and solute transport at the seawater/freshwater interface of a sandy aquifer.

777 *Geochimica et Cosmochimica Acta*, 69(16), 3979-3994.
778 doi:<https://doi.org/10.1016/j.gca.2005.03.017>

779 Anderson, D. M., Glibert, P. M., & Burkholder, J. M. (2002). Harmful algal blooms and
780 eutrophication: nutrient sources, composition, and consequences. *Estuaries*,
781 25(4), 704-726.

782 Appelo, C. A. J., & Postma, D. (2005). Geochemistry. *Groundwater and pollution*, 536.

783 Appelo, C. A. J., & Willemsen, A. (1987). Geochemical calculations and observations on
784 salt water intrusions, I. A combined geochemical/minxing cell model. *Journal of*
785 *Hydrology*, 94(3-4), 313-330.

786 Armstrong, F. A. J. (1957). The iron content of sea water. *Journal of the Marine*
787 *Biological Association of the United Kingdom*, 36(3), 509-517.

788 Back, W., Hanshaw, B. B., Herman, J. S., & Van Driel, J. N. (1986). Differential
789 dissolution of a Pleistocene reef in the ground-water mixing zone of coastal
790 Yucatan, Mexico. *Geology*, 14(2), 137-140.

791 Barker, A. P., Newton, R. J., Bottrell, S. H., & Tellam, J. H. (1998). Processes affecting
792 groundwater chemistry in a zone of saline intrusion into an urban sandstone
793 aquifer. *Applied Geochemistry*, 13(6), 735-749.
794 doi:[https://doi.org/10.1016/S0883-2927\(98\)00006-7](https://doi.org/10.1016/S0883-2927(98)00006-7)

795 Barker, S., & Ridgwell, A. (2012). Ocean acidification. *Nature Education Knowledge*,
796 3(10), 21.

797 Bristow, L. A., Mohr, W., Ahmerkamp, S., & Kuypers, M. M. M. (2017). Nutrients that
798 limit growth in the ocean. *Current Biology*, 27(11), R474-R478.

799 Brown, C. J., Coates, J. D., & Schoonen, M. A. A. (1999). Localized Sulfate-Reducing
800 Zones in a Coastal Plain Aquifer. *Groundwater*, 37(4), 505-516.

801 Burnett, B. (1999). Offshore springs and seeps are focus of working group. *Eos*,
802 *Transactions American Geophysical Union*, 80(2), 13-15.

803 Burnett, W. C. (1996). Tracing groundwater flow into surface waters using natural super
804 (222)Rn. *LOICZ Reports Studies*(8), 22-36.

805 Burnett, W. C., Bokuniewicz, H., Huettel, M., Moore, W. S., & Taniguchi, M. (2003).
806 Groundwater and pore water inputs to the coastal zone. *Biogeochemistry*, 66(1),
807 3-33.

808 Burnett, W. C., Taniguchi, M., & Oberdorfer, J. (2001). Measurement and significance
809 of the direct discharge of groundwater into the coastal zone. *Journal of Sea*
810 *Research*, 46(2), 109-116.

811 Canfield, D. (2001). Biogeochemistry of sulfur isotopes. *Reviews in mineralogy and*
812 *geochemistry*, 43(1), 607-636.

813 Carrera, J., Vázquez-Suñé, E., Castillo, O., & Sánchez-Vila, X. (2004). A methodology
814 to compute mixing ratios with uncertain end-members. *Water Resources*
815 *Research*, 40(12).

816 Cerdà-Domènech, M., Rodellas, V., Folch, A., & Garcia-Orellana, J. (2017).
817 Constraining the temporal variations of Ra isotopes and Rn in the groundwater
818 end-member: Implications for derived SGD estimates. *Science of the total*
819 *environment*, 595, 849-857.

820 Custodio, E. (1992). Coastal aquifer salinization as a consequence of aridity: the case of
821 Amurga phonolitic massif, Gran Canaria Island. *Study and Modelling of Salwater*
822 *Intrusion, CIMNE-UPC, Barcelona*, 81-98.

823 Chapelle, F. H., & Lovley, D. R. (1992). Competitive exclusion of sulfate reduction by
824 Fe (III)-reducing bacteria: a mechanism for producing discrete zones of high-iron
825 ground water. *Groundwater*, 30(1), 29-36.

- 826 Chatton, E., Aquilina, L., Pételet-Giraud, E., Cary, L., Bertrand, G., Labasque, T., . . .
827 Pauwels. (2016). Glacial recharge, salinisation and anthropogenic contamination
828 in the coastal aquifers of Recife (Brazil). *Science of The Total Environment*, 569-
829 570, 1114-1125. doi:<https://doi.org/10.1016/j.scitotenv.2016.06.180>
- 830 Chen, X., Cukrov, N., Santos, I. R., Rodellas, V., Cukrov, N., & Du, J. (2020). Karstic
831 submarine groundwater discharge into the Mediterranean: Radon-based nutrient
832 fluxes in an anchialine cave and a basin-wide upscaling. *Geochimica et*
833 *Cosmochimica Acta*, 268, 467-484.
- 834 Christophersen, N., Neal, C., Hooper, R. P., Vogt, R. D., & Andersen, S. (1990).
835 Modelling streamwater chemistry as a mixture of soilwater end-members—a step
836 towards second-generation acidification models. *Journal of Hydrology*, 116(1-4),
837 307-320.
- 838 Church, P. E., & Granato, G. E. (1996). Bias in ground-water data caused by well-bore
839 flow in long-screen wells. *Groundwater*, 34(2), 262-273.
- 840 Davis, S. N., & DeWiest, R. J. M. (1966). Hydrogeology John Wiley Sons New York
841 NY.
- 842 De Simoni, M., Carrera, J., Sanchez-Vila, X., & Guadagnini, A. (2005). A procedure for
843 the solution of multicomponent reactive transport problems. *Water Resources*
844 *Research*, 41(11).
- 845 Diego-Feliu, M., Rodellas, V., Saaltink, M. W., Alorda-Kleinglass, A., Goyetche, T.,
846 Martínez-Pérez, L., . . . Garcia-Orellana, J. (2021). New perspectives on the use
847 of ²²⁴Ra/²²⁸Ra and ²²²Rn/²²⁶Ra activity ratios in groundwater studies. *Journal*
848 *of Hydrology*, 596, 126043. doi:10.1016/j.jhydrol.2021.126043
- 849 Duque, C., Russoniello, C. J., & Rosenberry, D. O. (2020). History and evolution of
850 seepage meters for quantifying flow between groundwater and surface water: Part
851 2—Marine settings and submarine groundwater discharge. *Earth-Science Reviews*,
852 204, 103168.
- 853 Eissa, M. A. (2018). Application of multi-isotopes and geochemical modeling for
854 delineating recharge and salinization sources in Dahab Basin aquifers (South
855 Sinai, Egypt). *Hydrology*, 5(3), 41.
- 856 Fleury, P., Bakalowicz, M., & de Marsily, G. (2007). Submarine springs and coastal karst
857 aquifers: a review. *Journal of Hydrology*, 339(1-2), 79-92.
- 858 Folch, A., del Val, L., Luquot, L., Martínez-Pérez, L., Bellmunt, F., Le Lay, H., . . .
859 Carrera, J. (2020). Combining fiber optic DTS, cross-hole ERT and time-lapse
860 induction logging to characterize and monitor a coastal aquifer. *Journal of*
861 *Hydrology*, 588, 125050. doi:10.1016/j.jhydrol.2020.125050
- 862 Fratesi, B. (2013). Hydrology and geochemistry of the freshwater lens in coastal karst
863 *Coastal karst landforms* (pp. 59-75): Springer.
- 864 Gattuso, J. P., Frankignoulle, M., Bourge, I., Romaine, S., & Buddemeier, R. W. (1998).
865 Effect of calcium carbonate saturation of seawater on coral calcification. *Global*
866 *and Planetary Change*, 18(1-2), 37-46.
- 867 Giménez-Forcada, E. (2010). Dynamic of sea water interface using hydrochemical facies
868 evolution diagram. *Groundwater*, 48(2), 212-216.
- 869 Gomis-Yagües, V., Boluda-Botella, N., & Ruiz-Beviá, F. (2000). Gypsum
870 precipitation/dissolution as an explanation of the decrease of sulphate
871 concentration during seawater intrusion. *Journal of Hydrology*, 228(1-2), 48-55.
- 872 Grzelak, K., Tamborski, J., Kotwicki, L., & Bokuniewicz, H. (2018). Ecostructuring of
873 marine nematode communities by submarine groundwater discharge. *Marine*
874 *environmental research*, 136, 106-119.

- 875 Hanshaw, B. B., & Back, W. (1980). Chemical mass-wasting of the northern Yucatan
876 Peninsula by groundwater dissolution. *Geology*, 8(5), 222-224.
- 877 Hassen, I., Hamzaoui-Azaza, F., & Bouhlila, R. (2018). Establishing complex
878 compartments-aquifers connectivity via geochemical approaches towards
879 hydrogeochemical conceptual model: Kasserine Aquifer System, Central Tunisia.
880 *Journal of Geochemical Exploration*, 188, 257-269.
- 881 Hooper, R. P. (2003). Diagnostic tools for mixing models of stream water chemistry.
882 *Water Resources Research*, 39(3).
- 883 Hooper, R. P., Christophersen, N., & Peters, N. E. (1990). Modelling streamwater
884 chemistry as a mixture of soilwater end-members—An application to the Panola
885 Mountain catchment, Georgia, USA. *Journal of Hydrology*, 116(1-4), 321-343.
- 886 Hurrell, J. W., Holland, M. M., Gent, P. R., Ghan, S., Kay, J. E., Kushner, P. J., . . .
887 Lindsay, K. (2013). The community earth system model: a framework for
888 collaborative research. *Bulletin of the American Meteorological Society*, 94(9),
889 1339-1360.
- 890 Hutchins, S. R., & Acree, S. D. (2000). Ground water sampling bias observed in shallow,
891 conventional wells. *Groundwater Monitoring & Remediation*, 20(1), 86-93.
- 892 Jiao, J. J., & Post, V. (2019). *Coastal Hydrogeology*. Cambridge: Cambridge University
893 Press.
- 894 Jurado, A., Vázquez-Suñé, E., Carrera, J., Tubau, I., & Pujades, E. (2015). Quantifying
895 chemical reactions by using mixing analysis. *Science of The Total Environment*,
896 502, 448-456. doi:<https://doi.org/10.1016/j.scitotenv.2014.09.036>
- 897 Kendall, C., & Caldwell, E. A. (1998). Chapter 2 - Fundamentals of Isotope
898 Geochemistry. In C. Kendall & J. J. McDonnell (Eds.), *Isotope Tracers in*
899 *Catchment Hydrology* (pp. 51-86). Amsterdam: Elsevier.
- 900 Kim, J.-H., Kim, K.-H., Thao, N. T., Batsaikhan, B., & Yun, S.-T. (2017). Hydrochemical
901 assessment of freshening saline groundwater using multiple end-members mixing
902 modeling: A study of Red River delta aquifer, Vietnam. *Journal of Hydrology*,
903 549, 703-714. doi:<https://doi.org/10.1016/j.jhydrol.2017.04.040>
- 904 Kłostowska, Ż., Szymczycha, B., Lengier, M., Zarzeczańska, D., & Dzierzbicka-
905 Głowacka, L. (2020). Hydrogeochemistry and magnitude of SGD in the Bay of
906 Puck, southern Baltic Sea. *Oceanologia*, 62(1), 1-11.
907 doi:10.1016/j.oceano.2019.09.001
- 908 Kouzana, L., Mammou, A. B., & Felfoul, M. S. (2009). Seawater intrusion and associated
909 processes: Case of the Korba aquifer (Cap-Bon, Tunisia). *Comptes Rendus*
910 *Geoscience*, 341(1), 21-35. doi:10.1016/j.crte.2008.09.008
- 911 Liu, X., & Millero, F. J. (2002). The solubility of iron in seawater. *Marine Chemistry*,
912 77(1), 43-54.
- 913 Li, P., Wu, J., & Qian, H. (2016). Preliminary assessment of hydraulic connectivity
914 between river water and shallow groundwater and estimation of their transfer rate
915 during dry season in the Shidi River, China. *Environmental Earth Sciences*, 75(2).
916 doi:10.1007/s12665-015-4949-7
- 917 Liu, Y., Jiao, J. J., Liang, W., & Kuang, X. (2017). Hydrogeochemical characteristics in
918 coastal groundwater mixing zone. *Applied Geochemistry*, 85, 49-60.
919 doi:10.1016/j.apgeochem.2017.09.002
- 920 Liu, Y., Jiao, J. J., Liang, W., Santos, I. R., Kuang, X., & Robinson, C. E. (2021).
921 Inorganic carbon and alkalinity biogeochemistry and fluxes in an intertidal beach
922 aquifer: Implications for ocean acidification. *Journal of Hydrology*, 595, 126036.
923 doi:<https://doi.org/10.1016/j.jhydrol.2021.126036>

- 924 Long, A. J., & Valder, J. F. (2011). Multivariate analyses with end-member mixing to
 925 characterize groundwater flow: Wind Cave and associated aquifers. *Journal of*
 926 *Hydrology*, 409(1), 315-327. doi:10.1016/j.jhydrol.2011.08.028
- 927 Luijendijk, E., Gleeson, T., & Moosdorf, N. (2020). Fresh groundwater discharge
 928 insignificant for the world's oceans but important for coastal ecosystems. *Nature*
 929 *Communications*, 11(1). doi:10.1038/s41467-020-15064-8
- 930 Luo, X., & Jiao, J. J. (2016). Submarine groundwater discharge and nutrient loadings in
 931 Tolo Harbor, Hong Kong using multiple geotracer-based models, and their
 932 implications of red tide outbreaks. *Water research*, 102, 11-31.
- 933 Magaritz, M., Goldenberg, L., Kafri, U., & Arad, A. (1980). Dolomite formation in the
 934 seawater–freshwater interface. *Nature*, 287(5783), 622-624.
- 935 Mahlkecht, J., Merchán, D., Rosner, M., Meixner, A., & Ledesma-Ruiz, R. (2017).
 936 Assessing seawater intrusion in an arid coastal aquifer under high anthropogenic
 937 influence using major constituents, Sr and B isotopes in groundwater. *Science of*
 938 *The Total Environment*, 587, 282-295.
- 939 Martínez-Pérez, L., Luquot, L., Carrera, J., Marazuela, M. A., Goyetche, T., Pool, M., . . .
 940 . Folch, A. (2022). A multidisciplinary approach to characterizing coastal alluvial
 941 aquifers to improve understanding of seawater intrusion and submarine
 942 groundwater discharge. *Journal of Hydrology*, 127510.
- 943 Martínez, D., & Bocanegra, E. (2002). Hydrogeochemistry and cation-exchange
 944 processes in the coastal aquifer of Mar Del Plata, Argentina. *Hydrogeology*
 945 *Journal*, 10(3), 393-408.
- 946 McMahan, P. B., Chapelle, F. H., & Bradley, P. M. (2011). Evolution of redox processes
 947 in groundwater *Aquatic Redox Chemistry* (pp. 581-597): ACS Publications.
- 948 Milliman, J. D. (1993). Production and accumulation of calcium carbonate in the ocean:
 949 Budget of a nonsteady state. *Global Biogeochemical Cycles*, 7(4), 927-957.
- 950 Molins, S., Carrera, J., Ayora, C., & Saaltink, M. W. (2004). A formulation for decoupling
 951 components in reactive transport problems. *Water Resources Research*, 40(10).
- 952 Monastersky, R. (1996). Seep and ye shall find: Hidden water flow. *Science News*, 245-
 953 245.
- 954 Moore, W. S. (1999). The subterranean estuary: a reaction zone of ground water and sea
 955 water. *Marine Chemistry*, 65(1-2), 111-125. doi:10.1016/S0304-4203(99)00014-
 956 6
- 957 Moore, W. S. (2010). The Effect of Submarine Groundwater Discharge on the Ocean.
 958 *Annual Review of Marine Science*, 2(1), 59-88. doi:10.1146/annurev-marine-
 959 120308-081019
- 960 Morse, J. W., & Berner, R. A. (1995). What determines sedimentary C/S ratios?
 961 *Geochimica et Cosmochimica Acta*, 59(6), 1073-1077.
- 962 Nakaya, S., Uesugi, K., Motodate, Y., Ohmiya, I., Komiya, H., Masuda, H., & Kusakabe,
 963 M. (2007). Spatial separation of groundwater flow paths from a multi-flow system
 964 by a simple mixing model using stable isotopes of oxygen and hydrogen as natural
 965 tracers. *Water Resources Research*, 43(9).
- 966 Palacios, A., Ledo, J. J., Linde, N., Luquot, L., Bellmunt, F., Folch, A., . . . Martínez, L.
 967 (2020). Time-lapse cross-hole electrical resistivity tomography (CHERT) for
 968 monitoring seawater intrusion dynamics in a Mediterranean aquifer. *Hydrology*
 969 *and Earth System Sciences*, 24(4), 2121-2139.
- 970 Pelizardi, F., Bea, S. A., Carrera, J., & Vives, L. (2017). Identifying geochemical
 971 processes using End Member Mixing Analysis to decouple chemical components
 972 for mixing ratio calculations. *Journal of Hydrology*, 550, 144-156.

- 973 Peng, T., Zhu, Z., Du, J., & Liu, J. (2021). Effects of nutrient-rich submarine groundwater
974 discharge on marine aquaculture: A case in Lianjiang, East China Sea. *Science of*
975 *The Total Environment*, 147388.
- 976 Poulsen, D. L., Cook, P. G., Simmons, C. T., McCallum, J. L., & Dogramaci, S. (2019).
977 Effects of intraborehole flow on purging and sampling long-screened or open
978 wells. *Groundwater*, 57(2), 269-278.
- 979 Pulido-Leboeuf, P. (2004). Seawater intrusion and associated processes in a small coastal
980 complex aquifer (Castell de Ferro, Spain). *Applied Geochemistry*, 19(10), 1517-
981 1527.
- 982 Rezaei, M., Sanz, E., Raeisi, E., Ayora, C., Vázquez-Suñé, E., & Carrera, J. (2005).
983 Reactive transport modeling of calcite dissolution in the fresh-salt water mixing
984 zone. *Journal of Hydrology*, 311(1-4), 282-298.
- 985 Rosecrans, C. Z., Nolan, B. T., & Gronberg, J. M. (2017). Prediction and visualization of
986 redox conditions in the groundwater of Central Valley, California. *Journal of*
987 *Hydrology*, 546, 341-356.
- 988 Rufi-Salís, M., Garcia-Orellana, J., Cantero, G., Castillo, J., Hierro, A., Rieradevall, J., &
989 Bach, J. (2019). Influence of land use changes on submarine groundwater
990 discharge. *Environmental Research Communications*, 1(3), 031005.
991 doi:10.1088/2515-7620/ab1695
- 992 Russak, A., & Sivan, O. (2010). Hydrogeochemical Tool to Identify Salinization or
993 Freshening of Coastal Aquifers Determined from Combined Field Work,
994 Experiments, and Modeling. *Environmental Science & Technology*, 44(11), 4096-
995 4102. doi:10.1021/es1003439
- 996 Russak, A., Sivan, O., & Yechieli, Y. (2016). Trace elements (Li, B, Mn and Ba) as
997 sensitive indicators for salinization and freshening events in coastal aquifers.
998 *Chemical Geology*, 441, 35-46.
- 999 Rusydi, A. F., Onodera, S.-I., Saito, M., Ioka, S., Maria, R., Ridwansyah, I., & Delinom,
1000 R. M. (2021). Vulnerability of groundwater to iron and manganese contamination
1001 in the coastal alluvial plain of a developing Indonesian city. *SN Applied Sciences*,
1002 3(4), 1-12.
- 1003 Santos, I. R. S., Burnett, W. C., Chanton, J., Mwashote, B., Suryaputra, I. G. N. A., &
1004 Dittmar, T. (2008). Nutrient biogeochemistry in a Gulf of Mexico subterranean
1005 estuary and groundwater-derived fluxes to the coastal ocean. *Limnology and*
1006 *Oceanography*, 53(2), 705-718. doi:<https://doi.org/10.4319/lo.2008.53.2.0705>
- 1007 Sawyer, A. H., Michael, H. A., & Schroth, A. W. (2016). From soil to sea: the role of
1008 groundwater in coastal critical zone processes. *WIREs Water*, 3(5), 706-726.
1009 doi:<https://doi.org/10.1002/wat2.1157>
- 1010 Scott, G., & Crunkilton, R. L. (2000). Acute and chronic toxicity of nitrate to fathead
1011 minnows (*Pimephales promelas*), *ceriodaphnia dubia*, and *Daphnia magna*.
1012 *Environmental Toxicology and Chemistry*, 19(12), 2918-2922.
1013 doi:<https://doi.org/10.1002/etc.5620191211>
- 1014 Shalev, E., Lazar, A., Wollman, S., Kington, S., Yechieli, Y., & Gvirtzman, H. (2009).
1015 Biased Monitoring of Fresh Water-Salt Water Mixing Zone in Coastal Aquifers.
1016 *Groundwater*, 47(1), 49-56. doi:<https://doi.org/10.1111/j.1745-6584.2008.00502.x>
- 1017
- 1018 Shin, K., Koh, D.-C., Jung, H., & Lee, J. (2020). The Hydrogeochemical Characteristics
1019 of Groundwater Subjected to Seawater Intrusion in the Archipelago, Korea.
1020 *Water*, 12(6), 1542.
- 1021 Sivan, O., Yechieli, Y., Herut, B., & Lazar, B. (2005). Geochemical evolution and
1022 timescale of seawater intrusion into the coastal aquifer of Israel. *Geochimica et*

- 1023 *Cosmochimica Acta*, 69(3), 579-592.
 1024 doi:<https://doi.org/10.1016/j.gca.2004.07.023>
- 1025 Slomp, C. P., & Van Cappellen, P. (2004). Nutrient inputs to the coastal ocean through
 1026 submarine groundwater discharge: controls and potential impact. *Journal of*
 1027 *Hydrology*, 295(1), 64-86. doi:10.1016/j.jhydrol.2004.02.018
- 1028 Small, C., & Nicholls, R. J. (2003). A global analysis of human settlement in coastal
 1029 zones. *Journal of Coastal Research*, 584-599.
- 1030 Snyder, M., Taillefert, M., & Ruppel, C. (2004). Redox zonation at the saline-influenced
 1031 boundaries of a permeable surficial aquifer: effects of physical forcing on the
 1032 biogeochemical cycling of iron and manganese. *Journal of Hydrology*, 296(1),
 1033 164-178. doi:10.1016/j.jhydrol.2004.03.019
- 1034 Spotte, S. (1979). Fish and invertebrate culture: water management in closed systems-2.
 1035 Sutcliffe Jr, W. H. (1972). Some relations of land drainage, nutrients, particulate material,
 1036 and fish catch in two eastern Canadian bays. *Journal of the Fisheries Board of*
 1037 *Canada*, 29(4), 357-362.
- 1038 Taniguchi, M., Dulai, H., Burnett, K. M., Santos, I. R., Sugimoto, R., Stieglitz, T., . . .
 1039 Burnett, W. C. (2019). Submarine groundwater discharge: updates on its
 1040 measurement techniques, geophysical drivers, magnitudes, and effects. *Frontiers*
 1041 *in Environmental Science*, 7, 141.
- 1042 Tubau, I., Vázquez-Suñé, E., Jurado, A., & Carrera, J. (2014). Using EMMA and MIX
 1043 analysis to assess mixing ratios and to identify hydrochemical reactions in
 1044 groundwater. *Science of The Total Environment*, 470-471, 1120-1131.
 1045 doi:10.1016/j.scitotenv.2013.10.121
- 1046 U. S. Environmental Protection Agency. (1986). *Quality criteria for water* (EPA 440/5-
 1047 86-0013). Retrieved from Washington, DC.:
- 1048 Valiela, I., Costa, J., Foreman, K., Teal, J. M., Howes, B., & Aubrey, D. (1990). Transport
 1049 of groundwater-borne nutrients from watersheds and their effects on coastal
 1050 waters. *Biogeochemistry*, 10(3), 177-197. doi:10.1007/BF00003143
- 1051 van Hulst, M., Dutay, J. C., Middag, R., de Baar, H., Roy-Barman, M., Gehlen, M.,
 1052 Tagliabue, A. & Sterl, A. (2016). Manganese in the world ocean: A first global
 1053 model. *Biogeosciences Discuss*, 14, 1-38.
- 1054 Velasco, J., Lloret, J., Millán, A., Marin, A., Barahona, J., Abellán, P., & Sánchez-
 1055 Fernández, D. (2006). Nutrient and particulate inputs into the Mar Menor lagoon
 1056 (SE Spain) from an intensive agricultural watershed. *Water, Air, and Soil*
 1057 *Pollution*, 176(1), 37-56.
- 1058 Vázquez-Suñé, E., Carrera, J., Tubau, I., Sánchez-Vila, X., & Soler, A. (2010). An
 1059 approach to identify urban groundwater recharge. *Hydrology and Earth System*
 1060 *Sciences*, 14(10), 2085-2097. doi:10.5194/hess-14-2085-2010
- 1061 Wicks, C. M., & Herman, J. S. (1996). Regional hydrogeochemistry of a modern coastal
 1062 mixing zone. *Water Resources Research*, 32(2), 401-407.
- 1063 Wigley, T. M. L., & Plummer, L. N. (1976). Mixing of carbonate waters. *Geochimica et*
 1064 *Cosmochimica Acta*, 40(9), 989-995. doi:10.1016/0016-7037(76)90041-7
- 1065 Wilkinson, B. H., & Algeo, T. J. (1989). Sedimentary carbonate record of calcium-
 1066 magnesium cycling. *American Journal of Science*, 289(10), 1158-1194.
- 1067 Windom, H. L., Moore, W. S., Niencheski, L. F. H., & Jahnke, R. A. (2006). Submarine
 1068 groundwater discharge: A large, previously unrecognized source of dissolved iron
 1069 to the South Atlantic Ocean. *Marine Chemistry*, 102(3), 252-266.
 1070 doi:10.1016/j.marchem.2006.06.016

1071